The Astrophysical Journal, 899:26 (19pp), 2020 August 10 https://doi.org/10.3847/1538-4357/aba2cc

Spin Evolution of Stellar-mass Black Hole Binaries in Active Galactic Nuclei

Hiromichi Tagawa[1,2], Zoltán Haiman[3], Imre Bartos[4], and Bence Kocsis[2,5]
[1] Astronomical Institute, Graduate School of Science, Tohoku University, Aoba, Sendai 980-8578, Japan; htagawa@caesar.elte.hu
[2] Institute of Physics, Eötvös University, Pázmány P.s., Budapest, 1117, Hungary
[3] Department of Astronomy, Columbia University, 550 W. 120th St., New York, NY 10027, USA
[4] Department of Physics, University of Florida, P.O. Box 118440, Gainesville, FL 32611, USA
[5] Rudolf Peierls Centre for Theoretical Physics, Clarendon Laboratory, Parks Road, Oxford, OX1 3PU, UK
Received 2020 April 24; revised 2020 June 19; accepted 2020 July 2; published 2020 August 10

Abstract

The astrophysical origin of gravitational-wave (GW) events is one of the most timely problems in the wake of the LIGO/Virgo discoveries. In active galactic nuclei (AGNs), binaries form and evolve efficiently by dynamical interactions and gaseous dissipation. Previous studies have suggested that binary black hole (BBH) mergers in AGN disks can contribute significantly to BBH mergers observed by GW interferometers. Here we examine the distribution of the effective spin parameter $\chi_{\rm eff}$ of this GW source population. We extend our semi-analytical model of binary formation and evolution in AGN disks by following the evolution of the binary orbital angular momenta and black hole (BH) spins. BH spins change due to gas accretion and BH mergers, while the binary orbital angular momenta evolve due to gas accretion and binary–single interactions. We find that the distribution of $\chi_{\rm eff}$ predicted by our AGN model is similar to the distribution observed during LIGO/Virgo O1 and O2. On the other hand, if radial migration of BHs is inefficient, $\chi_{\rm eff}$ is skewed toward higher values than the observed distribution, because of the paucity of scattering events that would randomize spin directions relative to the orbital plane. We suggest that high binary masses and the positive correlation between binary mass and the standard deviation of $\chi_{\rm eff}$ for chirp masses up to $\approx 20\,M_{\odot}$ can be possible signatures for mergers originating in AGN disks. Finally, hierarchical mergers in AGN disks naturally produce properties of the recent GW event GW190412, including a low mass ratio, a high primary BH spin, and a significant spin component in the orbital plane.

Unified Astronomy Thesaurus concepts: Gravitational wave sources (677); Active galactic nuclei (16); Stellar mass black holes (1611)

1. Introduction

Recent detections of gravitational waves (GWs) have shown evidence for a high rate of black hole (BH)–BH and neutron star (NS)–NS mergers in the universe (The LIGO Scientific Collaboration et al. 2019; Venumadhav et al. 2019). However, the proposed astrophysical pathways to mergers remain highly debated. Indeed there are currently an exceedingly large number of such possible pathways, with widely different environments and physical processes. A comprehensive list of these currently includes isolated binary evolution (e.g., Dominik et al. 2012; Kinugawa et al. 2014; Belczynski et al. 2016; Spera et al. 2019) accompanied by mass transfer (Inayoshi et al. 2017a; Pavlovskii et al. 2017; van den Heuvel et al. 2017), common envelope ejection (e.g., Paczynski 1976; Ivanova et al. 2013), envelope expansion (Tagawa et al. 2018), chemically homogeneous evolution in a tidally distorted binary (de Mink & Mandel 2016; Mandel & de Mink 2016; Marchant et al. 2016), evolution of triple or quadruple systems (e.g., Antonini et al. 2017; Silsbee & Tremaine 2017), gravitational capture (e.g., O'Leary et al. 2009; Gondán et al. 2018; Rasskazov & Kocsis 2019), dynamical evolution in open clusters (e.g., Banerjee 2017; Kumamoto et al. 2018) and dense star clusters (e.g., Portegies Zwart & McMillan 2000; Samsing et al. 2014; O'Leary et al. 2016; Rodriguez et al. 2016; di Carlo et al. 2019), and dynamical interaction in a gas-rich nuclear region (e.g., Bartos et al. 2017b; Stone et al. 2017; McKernan et al. 2018; Tagawa et al. 2020).

Galactic nuclei are the densest environments of stars and compact objects in the universe (see Neumayer et al. 2020, for a recent review). In an active galactic nucleus (AGN), a high-density gas disk forms within 0.1–10 pc (Burtscher et al. 2013) around a central supermassive BH (SMBH). Several authors have recently pointed out that these environments are conducive to forming compact-object binaries. This "AGN disk channel" has received increasing attention in the wake of the LIGO/Virgo discoveries, as a possible explanation for some of the LIGO/Virgo events. In particular, McKernan et al. (2012, 2014) predicted the formation of intermediate-mass BHs in AGN disks due to collisions of compact objects. Bartos et al. (2017b) have proposed a pathway for binary BH (BBH) mergers in AGN disks in which binaries are captured by an accretion disk within ∼0.01 pc from the SMBH due to linear momentum exchange during disk-crossing, and after that, binaries are hardened by gas dynamical friction with an AGN disk and type I/II torques from circumbinary disks. Stone et al. (2017) have proposed another pathway, in which binaries formed in situ at the scale of about a parsec evolve via binary–single interactions with a disk stellar component and type I/II torques from circumbinary disks. Leigh et al. (2018) showed that fewer than ten binary–single interactions are sufficient to drive hard binaries with a binary separation of $s \lesssim 10$ au to merger. McKernan et al. (2020) investigated the evolution of NSs and white dwarfs in addition to BHs, and estimated the rate of mergers among these objects. Ford & McKernan (2019) suggested that the AGN models can be constrained from GW observations. Bellovary et al. (2016) suggested that BHs accumulate and merge with each other in migration traps at 20–300 Schwarzschild radii from the central SMBH, where the sign of the torque from the AGN disk

changes. Secunda et al. (2019), Yang et al. (2019a, 2019b), and Gayathri et al. (2020) investigated the properties of mergers in migration traps. Tagawa et al. (2020) investigated how binaries form and merge in AGN disks by performing self-consistent one-dimensional N-body simulations combined with semi-analytical prescriptions of the relevant processes. They found that binaries form efficiently in the inner regions ($\lesssim$1 pc, but well outside the migration traps) of AGN disks, due to the dissipation of relative velocities of unbound pairs of BHs via gas drag ("gas-capture" binaries), and merge at $\sim$0.01 pc from the SMBH, where gaps form around BHs and so interactions among compact objects become frequent, similarly to migration traps.

Motivated by the above, in the present paper we investigate whether the AGN disk channel can be distinguished from other formation pathways. Previous work proposed distinguishing features based on spatial associations with bright AGNs (Bartos et al. 2017a; Corley et al. 2019), large chirp masses (Tagawa et al. 2020), redshift evolution (Yang et al. 2020), acceleration of the binary's center of mass (Inayoshi et al. 2017b; Meiron et al. 2017; Wong et al. 2019), or gravitational lensing (Kocsis 2013; D'Orazio & Loeb 2020). One feature that has not yet been studied in detail in this channel is the expected distribution of BH spins. The effective spin parameter $\chi_{\rm eff}$ (which is the sum of the projection of binary spins onto the binary orbital angular momentum) has been shown to provide useful information to constrain other compact-object merger pathways (Stevenson et al. 2017; Talbot & Thrane 2017; Vitale et al. 2017).

The $\chi_{\rm eff}$ distribution inferred from the observed GW events prefers low values (The LIGO Scientific Collaboration et al. 2019), which suggests low natal BH spins or random directions between the binary orbital angular momentum and the BH spins (Farr et al. 2017). On the other hand, several events are reported to have high or low $\chi_{\rm eff}$ values (Zackay et al. 2019, 2020; The LIGO Scientific Collaboration and The Virgo Collaboration 2020). Safarzadeh et al. (2020) suggested that there is a negative and a positive correlation between mass and the mean and the dispersion of $\chi_{\rm eff}$, respectively. For the evolution of isolated binaries, the low observed $\chi_{\rm eff}$ values may be reproduced if the angular momentum transport within the stars is highly efficient (Qin et al. 2018; Bavera et al. 2020). In globular clusters, the orbital angular momentum directions of binaries are randomized by binary–single interactions, which predicts a $\chi_{\rm eff}$ distribution symmetric around $\chi_{\rm eff}=0$ and favoring low values (Arca-Sedda et al. 2018; Rodriguez et al. 2018). For triple systems, the Kozai mechanism can cause misalignment of BH spins (Liu & Lai 2017, 2018; Liu et al. 2019; Fragione & Kocsis 2020).

Several recent studies have investigated the properties (e.g., $\chi_{\rm eff}$, mass ratio, binary mass) of binary mergers in AGN disks. For mergers in migration traps, Yang et al. (2019a, 2019b) and McKernan et al. (2019) performed Monte Carlo simulations, and predicted that typical mergers have a low mass ratio of $q\sim0.2$ and significant effective spin $|\chi_{\rm eff}|\sim0.4$. Gayathri et al. (2020) showed that mergers in migration traps can explain the values of $\chi_{\rm eff}$ and $m_{\rm chirp}$ for GW170817A. Secunda et al. (2019, 2020) investigated the dynamical evolution of compact objects around migration traps by directly following their orbits in numerical simulations.

Focusing on mergers occurring outside migration traps, McKernan et al. (2019) estimated the mass and spin distribution for mergers among binaries formed during close encounters in AGN disks, by assuming that binaries are always aligned or anti-aligned with the AGN disk, and BH mergers are much faster than the growth of BH spins by gas accretion. They found that the distribution of $\chi_{\rm eff}$ is symmetric around zero, and the dispersion of $\chi_{\rm eff}$ is determined by the magnitude of initial BH spins. They predicted a variety of the merged mass distribution depending on adopted initial mass functions (IMFs), which are roughly consistent with results by Tagawa et al. (2020, hereafter Paper I). However, in Paper I, BH mergers were found to be less rapid, because gas dynamical friction becomes inefficient as the binary separation shrinks, and because that paper employed an updated version of type I/II migration theory, which predicts weaker torques than previous versions (e.g., Duffell et al. 2014; Kanagawa et al. 2018). Also, Paper I suggested that the orbital angular momenta of the binaries at mergers are often misaligned with the AGN disk due to frequent hard binary–single interactions. Since the merger timescale of BBHs is comparable to the timescale of gas accretion onto BHs, the evolution of the BH spins needs to be explicitly followed, accounting for both effects. Furthermore, to determine the $\chi_{\rm eff}$ distribution for mergers in AGN disks, it is necessary to also follow the orbital angular momenta of the binaries, again taking into account both binary–single interactions and gas accretion.

In this paper, we determine the distribution of $\chi_{\rm eff}$ for binary mergers in AGN disks by incorporating the evolution of BH spins and the binary orbital angular momenta into the semi-analytical prescriptions and one-dimensional N-body simulations used in Paper I. We find that the frequency of binary–single interactions, the angular momentum of the captured gas, and the initial BH spin directions strongly influence the $\chi_{\rm eff}$ distribution. The rest of this paper is organized as follows. In Section 2, we describe the numerical scheme and the setup of the simulations. We present our main results in Section 3, and summarize our conclusions in Section 4.

2. Method

To derive the $\chi_{\rm eff}$ distribution at mergers, the evolution of the dimensionless BH spins ($\boldsymbol{a}$) and the binary orbital angular momentum directions ($\hat{\boldsymbol{J}}_{\rm bin}$)[6] needs to be followed since $\chi_{\rm eff}$ is the sum of the projection of mass-weighted binary spins onto the binary orbital angular momentum,

$$\chi_{\rm eff}=\frac{m_1\boldsymbol{a}_1+m_2\boldsymbol{a}_2}{m_1+m_2}\cdot\hat{\boldsymbol{J}}_{\rm bin}. \quad (1)$$

Here m_1 and m_2 are the masses and $\boldsymbol{a}_1$ and $\boldsymbol{a}_2$ are the spins of the binary components. To model the evolution of the BH spins and the binary orbital angular momenta, we perform one-dimensional N-body simulations combined with semi-analytical prescriptions. In the following sections, we first give a brief overview of our model and then describe its ingredients in more detail.

2.1. Overview of the Model

In this section, we summarize our model, whose details are presented in Paper I. We consider a system describing a galactic nucleus, consisting of the following five components: (1) a central SMBH, (2) a gaseous accretion disk around the SMBH ("AGN disk"), (3) a spherical stellar cluster, (4) a

[6] We use the usual notation for unit vectors $\hat{\boldsymbol{x}}=\boldsymbol{x}/|\boldsymbol{x}|$.

Table 1
Fiducial Values of Our Model Parameters

Parameter	Fiducial Value
Initial BH spin magnitude	$\lvert\boldsymbol{a}\rvert = 0$
Angular momentum directions of circum-BH disks	$\hat{\boldsymbol{J}}_{\rm CBHD} = \hat{\boldsymbol{J}}_{\rm AGN}$ for single BHs, $\hat{\boldsymbol{J}}_{\rm CBHD} = \hat{\boldsymbol{J}}_{\rm bin}$ for BHs in binaries
Ratio of viscous parameters	$\nu_2/\nu_1 = 10$
Efficiency of alignment of $\boldsymbol{J}_{\rm bin}$ due to gas capture	$f_{\rm rot} = 1$
Mass of the central SMBH	$M_{\rm SMBH} = 4 \times 10^6\,M_\odot$
Gas accretion rate at the outer radius	$\dot{M}_{\rm out} = 0.1\,\dot{M}_{\rm Edd}$
Fraction of pre-existing binaries	$f_{\rm pre} = 0.15$
Power-law exponent for the initial density profile for BHs	$\gamma_\rho = 0$
Parameter setting the initial velocity anisotropy for BHs	$\beta_{\rm v} = 0.2$
Efficiency of angular momentum transport in the α-disk	$\alpha_{\rm SS} = 0.1$
Stellar mass within 3 pc	$M_{\rm star,3pc} = 10^7\,M_\odot$
Stellar IMF slope	$\delta_{\rm IMF} = 2.35$
Angular momentum transfer parameter in the outer disk	$m_{\rm AM} = 0.15$
Accretion rate in Eddington units onto stellar-mass BHs	$\Gamma_{\rm Edd,cir} = 1$
Numerical time-step parameter	$\eta_t = 0.1$
Number of radial cells storing physical quantities	$N_{\rm cell} = 120$
Minimum and maximum r for the initial BH distribution	$r_{\rm in,BH} = 10^{-4}$ pc, $r_{\rm out,BH} = 3$ pc

flattened cluster of BHs, and (5) stars and BHs inside the AGN disk, referred to as the "disk stellar" and "disk BH" components. To follow the time evolution of the BHs in this system, focusing on their capture by the disk, and the formation, evolution, and disruption of BH binaries in the disk, we run one-dimensional N-body simulations combined with a semi-analytical method. We introduce N-body particles representing either single objects or binaries, and for each particle we follow its radial position from the central SMBH, as well as its radial velocity, together with the evolution of the binaries' separation. The other two spatial directions are followed only statistically. In this paper, we additionally follow the evolution of BH spins (Section 2.2) and the orbital angular momentum directions of binaries (Section 2.3).

For the AGN disk, we employ the model proposed by Thompson et al. (2005), as adopted in the earlier work by Stone et al. (2017). This represents a Shakura–Sunyaev α-disk with a constant viscosity parameter α and accretion rate in the region where it is not self-gravitating. The model describes a radiatively efficient, geometrically thin, and optically thick disk and extends the disk to parsec scales with a constant Toomre parameter in the self-gravitating regime, assuming that it is heated and stabilized by radiation pressure and supernovae from in situ star formation. We assume that stars and BHs form in the disk at the rate required to stabilize the AGN disk, and some fraction of BHs are initially formed in binaries (see parameter settings in Table 1).

We assume that the AGN disk is surrounded by a spherically symmetric star cluster, with a total mass $\approx$3 times that of the central SMBH within $\sim$3 pc, and with a density profile matching those of a nuclear cluster observed in the Galactic center. We further include a flattened BH cluster component, which has a steeper density profile and a smaller velocity dispersion than those of a spherically symmetric star cluster due to mass segregation (e.g., Hopman & Alexander 2006; Szolgyen & Kocsis 2018).

Our model tracks the properties of the BH population, including physical processes due both to the presence of gas and to multi-body dynamical interactions, as follows.

For the interaction with gas, the velocities of all BHs relative to the local AGN disk decrease due to accretion torque and to gas dynamical friction. For binaries of stellar-mass BHs, the binary separation evolves due to gas dynamical friction from the AGN disk and to type I/II migration torque from a small circumbinary disk that forms within the Hill sphere of the binary. Binaries efficiently form in the disk due to gas dynamical friction during two-body encounters (a process we dubbed "gas-capture binary formation"). The radial positions of BHs are also allowed to evolve due to type I/II torques from the AGN disk. Gas accretion affects BH spins and the orbital angular momentum directions of binaries according to newly added prescriptions (Sections 2.2.2 and 2.3.2, respectively).

We also account for dynamical interactions with single stars and BHs and BH binaries. The binaries' separations and velocities evolve due to binary–single interactions, and the velocities of all BHs additionally evolve due to scattering. The evolution of the orbital angular momentum directions of binaries during binary–single interactions is additionally followed with newly added prescriptions (Section 2.3.3). Binaries form due to three-body encounters, and are disrupted by soft binary–single interactions. We also account for GW emission from binaries, which reduces their separation rapidly once they are sufficiently tight. For simplicity, the evolution of eccentricity is ignored and orbits around the SMBH and binary orbits are both assumed to be circular.

The interested reader is encouraged to consult Paper I for detailed descriptions of the above model and its ingredients. In the following sections, we only describe the new prescriptions that we added to Paper I, in order to follow the evolution of $\chi_{\rm eff}$ of each BH binary.

2.2. BH Spin Evolution

BH spin is characterized by the dimensionless spin parameter $\boldsymbol{a} = c\boldsymbol{J}_{\rm BH}/Gm_{\rm BH}^2$, where G is the gravitational constant, c is the speed of light, $m_{\rm BH}$ is the mass of the BH, and $\boldsymbol{J}_{\rm BH}$ is its angular momentum. In this section, we describe the initial distribution and the subsequent evolution of BH spins.

2.2.1. Initial BH Spin Distribution

In our model, there are two types of BHs differentiated by their origin: BHs formed before the beginning of the current AGN phase (pre-existing BHs) and BHs formed during the current AGN phase (BHs formed in situ). Pre-existing BHs are distributed in nuclear star clusters, but have a density profile that is steeper (e.g., Freitag et al. 2006; Hopman & Alexander 2006; Keshet et al. 2009) and velocity dispersion that is smaller (Szolgyen & Kocsis 2018) than those of typical-mass stars. Pre-existing BHs are expected to have random spin directions since they presumably formed by the disruption of globular clusters (e.g., Mapelli & Gualandris 2016) or by the fragmentation of previous AGN disks or disks in non-active phases whose orientations differed from the current one.

On the other hand, BHs form in situ in the outer regions of the AGN disk, and could have their spins directed parallel to the angular momentum of the AGN disk. This may be expected if these BHs form from, or efficiently accrete, gas whose angular momentum direction is the same as that of the background AGN disk. This assertion might be justified by the analogy with the planets in the solar system, all of which except for Venus and Uranus spin in the same direction as their orbital motion to within 30°.

The typical values of the initial BH spins are highly uncertain. The progenitors of some BBHs, BHs in high-mass X-ray binaries, are observed to have high spin (see, e.g., Miller & Miller 2015 for a review). However, we do not have any information on the spins of isolated single BHs or for heavier BHs with masses similar to those discovered by GW observations.

We therefore consider several distributions for the initial BH spin $\boldsymbol{a}$. For the direction of the initial BH spin $\hat{\boldsymbol{a}}$, we examine two models: (i) the spin direction $\hat{\boldsymbol{a}}$ is random, (ii) $\hat{\boldsymbol{a}}$ is directed parallel to the angular momentum of the AGN disk $\hat{\boldsymbol{J}}_{\rm AGN}$ (the latter defined with respect to the SMBH), where we fix $\hat{\boldsymbol{J}}_{\rm AGN} = \hat{\boldsymbol{z}}$, i.e., along the z-axis. For the magnitude of the initial BH spin $|\boldsymbol{a}|$, we examine the full range of values between 0 and 0.99 (models M1–M7; see Table 2 below). In the fiducial model (M1), $a_0 = 0$ for both pre-existing BHs and those formed in situ (e.g., Fuller & Ma 2019). In models M2–M7, we instead assume $a_0 = 0.1$–0.99, respectively. In all six models M2–M7, the spin directions of the pre-existing BHs and those formed in situ were assumed to be random and aligned with the AGN disk, respectively. In models M8 and M9, we adopt $a_0 = 0.7$ for all BHs (e.g., Shibata & Shapiro 2002), but assume that *all* BH spins are random (model M8) or aligned with the AGN disk (model M9).

Note that in our models the initial BH mass is below 15 $M_\odot$, which may be expected for high-metallicity environments such as AGNs. Unlike in other BH formation channels with heavier BHs (e.g., Gerosa et al. 2018), at these lower masses there is no a priori anticorrelation between mass and spin. The BH masses and spins change significantly from their initial values during the evolution in AGNs due to gas accretion and mergers in our simulations.

2.2.2. Gas Accretion

In our model, BHs capture gas from the AGN disk while they are moving in or crossing the disk. Some fraction of captured gas is assumed to accrete onto BHs through circum-BH disks (for single BHs) or mini-disks (for BBHs, fed from circumbinary disks). During such accretion processes the binary mass, velocity, and separation, as well as the BH spins, all evolve.

The spin values $a = 1$ and -1 represent a maximally spinning BH, and the sign of a is defined so that for $a > 0$ the BH is spinning in the same direction as the inner accretion disk, and for $a < 0$ the spin is in the opposite direction. The spin magnitude after an accretion episode is given by

$$a^{\rm f} = \frac{1}{3}\frac{r_{\rm isco}^{1/2}}{f_{\rm acc}}\left[4 - \left(3\frac{r_{\rm isco}}{f_{\rm acc}^2} - 2\right)^{1/2}\right] \quad (2)$$

(Bardeen 1970), where $f_{\rm acc} \equiv (m_{\rm BH} + \Delta m_{\rm BH})/m_{\rm BH}$, $\Delta m_{\rm BH} \equiv \dot{m}_{\rm BH}\Delta t$ is the mass accreted during the time step Δt, the superscript f stands for the values after the episode, and $r_{\rm isco}$ is the radius of the innermost stable circular orbit (ISCO) in reduced units, defined as

$$r_{\rm isco} = R_{\rm isco}/R_{\rm g} = 3 + Z_2 \mp \sqrt{(3 - Z_1)(3 + Z_1 + 2Z_2)} \quad (3)$$

with the minus sign for $a > 0$ and the plus sign for $a < 0$. Here $R_{\rm g} = Gm_{\rm BH}/c^2$ is the gravitational radius of the BH, and the functions Z_1 and Z_2 are given by

$$Z_1 = 1 + (1 - |a|^2)^{1/3}[(1 + |a|)^{1/3} + (1 - |a|)^{1/3}], \quad (4)$$

$$Z_2 = \sqrt{3|a|^2 + Z_1^2}. \quad (5)$$

While Equation (2) gives unphysical spin values when a highly spinning BH accretes a significant amount of gas ($a^{\rm f} > 1$ or imaginary), the torque exerted by the radiation of a thin accretion disk prevents $a^{\rm f} > 0.998$ (Thorne 1974). Fully relativistic magnetohydrodynamics simulations suggest that the spin value does not grow beyond 0.95 during accretion from a thick disk (Gammie et al. 2004; Shapiro 2005). We set the upper limit of $a^{\rm f}$ to 0.99 in our models.

When the spin angular momentum $\boldsymbol{J}_{\rm BH} = \boldsymbol{a}\sqrt{Gm_{\rm BH}^3 R_{\rm g}}$ of a BH is misaligned with its inner disk, the BH induces a Lense–Thirring precession in the misaligned disk elements, which causes the inner parts of the disk and the BH spin to align. The transition between aligned and misaligned annuli of the disk occurs at the so-called warp radius $R_{\rm warp}$. In each time step Δt in our model, $\boldsymbol{J}_{\rm BH}$ aligns with the initial spin angular momentum of the BH plus the angular momentum $\Delta\boldsymbol{J}_{\rm warp}$ of the disk within the warp radius: $\boldsymbol{J}_{\rm BH} \to \boldsymbol{J}_{\rm BH} + \Delta\boldsymbol{J}_{\rm warp}$. For a Shakura–Sunyaev disk, the warp radius is given by

$$R_{\rm warp}/R_{\rm S} = 3.6 \times 10^2 |a|^{5/8} m_{\rm BH}^{1/8} f_{\rm Edd}^{-1/4}\left(\frac{\nu_2}{\nu_1}\right)\alpha_{\rm SS}^{-1/2} \quad (6)$$

(e.g., Volonteri et al. 2007), where $f_{\rm Edd} = \dot{m}_{\rm BH}c^2/L_{\rm Edd}$ is the accretion rate in Eddington units (without a radiative efficiency), $L_{\rm Edd}$ is the Eddington luminosity, ν_1 is the viscosity responsible for transferring angular momentum in the accretion disk, ν_2 is the viscosity responsible for warp propagation, and $\alpha_{\rm SS}$ is the efficiency of angular momentum transport in the α-disk. We set $\Delta J_{\rm warp} = \Delta M_{\rm warp}\sqrt{Gm_{\rm BH}R_{\rm warp}}$ (e.g., Volonteri et al. 2007), where $\Delta M_{\rm warp}$ is the mass of the warped disk aligned with the BH spin during Δt. We set $\Delta M_{\rm warp} = \Delta m_{\rm BH}$, and $\Delta\hat{\boldsymbol{J}}_{\rm warp}$ points in the same direction as the angular momentum of the circum-BH disk $\hat{\boldsymbol{J}}_{\rm CBHD}$. After alignment, the magnitude of the BH spin evolves through gas accretion via Equation (2).

We note that whenever the condition

$$\cos\theta_{\rm BH,warp} < -\frac{\Delta J_{\rm warp}}{2J_{\rm BH}} \quad (7)$$

is satisfied, where $\theta_{\rm BH,warp}$ is the angle between $\boldsymbol{J}_{\rm BH}$ and $\Delta\boldsymbol{J}_{\rm warp}$, the accretion disk within $R_{\rm warp}$ becomes anti-aligned with the BH spin direction (King et al. 2005).

Due to the Lense–Thirring effect, the BH spin and the angular momentum of the circum-BH disk $\hat{\boldsymbol{J}}_{\rm CBHD}$ align faster than the rate at which the magnitude of the BH spin grows

Table 2
The Results in Different Models

Input		Output									
Model	Parameter	$\chi_{\rm eff,med}$	$\chi_{\rm eff,10}$	$\chi_{\rm eff,90}$	$\lvert\chi_{\rm eff}\rvert_{\rm med}$	$P_{{\rm KS},\chi_{\rm eff}}$	$P_{{\rm KS},m_{\rm chirp}}$	$P_{{\rm KS},\chi_{\rm eff},m_{\rm chirp}}$	$P_{{\rm KS,LV},\chi_{\rm eff}}$	$P_{{\rm KS,LV},m_{\rm chirp}}$	$\min_i K_{{\rm A,obs},i}$
M1	Fiducial	0.012	−0.29	0.33	0.15	0.53	0.25	0.12	0.10	0.35	0.050
M2	$a_0 = 0.1$	0.022	−0.31	0.36	0.17	0.44	0.18	0.091	0.088	0.25	0.052
M3	$a_0 = 0.2$	0.022	−0.35	0.37	0.19	0.68	0.15	0.069	0.14	0.23	0.078
M4	$a_0 = 0.3$	0.020	−0.37	0.43	0.21	0.59	0.14	0.033	0.15	0.18	0.12
M5	$a_0 = 0.5$	0.032	−0.43	0.47	0.26	0.54	0.060	0.022	0.12	0.12	0.15
M6	$a_0 = 0.7$	0.043	−0.47	0.55	0.29	0.41	0.18	0.036	0.093	0.28	0.21
M7	$a_0 = 0.99$	0.022	−0.57	0.63	0.34	0.31	0.19	0.030	0.061	0.26	0.18
M8	random $\hat{\boldsymbol{a}}_0$, $a_0 = 0.7$	0.036	−0.48	0.54	0.29	0.45	0.17	0.030	0.091	0.25	0.21
M9	$\boldsymbol{a}_0 = 0.7\hat{\boldsymbol{z}}$	0.018	−0.56	0.63	0.35	0.23	0.095	0.082	0.049	0.55	0.19
M10	$\nu_2/\nu_1 = 2$	0.021	−0.30	0.35	0.16	0.46	0.086	0.052	0.10	0.15	0.087
M11	$\nu_2/\nu_1 = 50$	0.017	−0.29	0.32	0.15	0.56	0.11	0.045	0.11	0.17	0.039
M12	$\hat{\boldsymbol{J}}_{\rm CBHD} = \hat{\boldsymbol{z}}$	0.012	−0.33	0.35	0.18	0.45	0.20	0.097	0.081	0.29	0.045
M13	$f_{\rm rot} = 0$	0.0026	−0.29	0.31	0.14	0.61	0.26	0.14	0.12	0.41	0.068
M14	$f_{\rm rot} = 10$	0.017	−0.31	0.32	0.16	0.62	0.24	0.092	0.14	0.28	0.075
M15	w/o gas mig.	0.12	−0.19	0.46	0.19	0.077	9.2×10^{-9}	6.5×10^{-6}	0.068	2.1×10^{-4}	9.8×10^{-6}
M16	No gas hard.	0.014	−0.32	0.35	0.17	0.75	0.55	0.036	0.19	0.11	0.054
M17	$\dot{M}_{\rm out} = \dot{M}_{\rm Edd}$	0.0095	−0.31	0.33	0.16	0.68	0.15	0.078	0.15	0.22	0.064
M18	$r_{\rm out,\ BH} = 0.3$ pc	0.0023	−0.29	0.30	0.15	0.23	0.020	0.021	0.036	0.057	0.021
M19	$M_{\rm SMBH} = 4 \times 10^7\ M_\odot$	0.017	−0.31	0.35	0.17	0.31	0.065	0.028	0.066	0.13	0.11
M20	$\delta_{\rm IMF} = -1.7$	0.032	−0.29	0.35	0.16	0.54	0.16	0.046	0.12	0.23	0.064
M21	$\beta_{\rm v} = 1$	−0.0046	-0.32	0.33	0.16	0.31	0.0014	0.0038	0.058	0.011	0.025
M22	$M_{\rm star,\ 3pc} = 3 \times 10^6 M_\odot$	0.016	−0.31	0.34	0.17	0.28	0.033	0.037	0.054	0.080	0.048
M23	$\gamma_\rho = 1.5$	0.017	−0.31	0.34	0.16	0.63	0.16	0.083	0.14	0.21	0.058
M24	twice $m_{\rm BH}$	0.041	−0.29	0.35	0.17	0.60	0.15	0.062	0.13	0.14	0.033
M1	$t = 3$ Myr	0.014	−0.23	0.28	0.12	0.87	0.18	0.26	0.24	0.43	0.031
M1	$t = 30$ Myr	0.016	−0.37	0.38	0.19	0.49	0.082	0.043	0.11	0.15	0.096

Note. The first two columns show the model number and indicate its variation from the fiducial model (M1). For example, in M16 ("No gas hard.") binaries are not hardened by gas interaction, and M15 ("w/o gas mig.") excludes type I/II torques and the resulting radial migration in the AGN disk. In the next four columns, $\chi_{\rm eff,med}$, $\chi_{\rm eff,10}$, and $\chi_{\rm eff,90}$ are the median, 10th percentile, and 90th percentile for the $\chi_{\rm eff}$ distribution, respectively, and we show the median for the $\lvert\chi_{\rm eff}\rvert$ distributions, in all of which observational errors are included. In the next three columns, $P_{{\rm KS},\chi_{\rm eff}}$, $P_{{\rm KS},m_{\rm chirp}}$, and $P_{{\rm KS},\chi_{\rm eff},m_{\rm chirp}}$ are, respectively, the KS probabilities that the all observed events were drawn from the $\chi_{\rm eff}$, $m_{\rm chirp}$, and joint ($\chi_{\rm eff}$, $m_{\rm chirp}$) distributions predicted in each model. In the next two columns, $P_{{\rm KS,LV},\chi_{\rm eff}}$ and $P_{{\rm KS,LV},m_{\rm chirp}}$ are the KS probabilities that the events reported by the LIGO/Virgo collaborations were drawn from the predicted $\chi_{\rm eff}$ and $m_{\rm chirp}$ distributions. In the last column, $\min_i K_{{\rm A,\ obs,\ }i}$ is the lowest value of the Bayes factor among all observed GW events, evaluated for each event between the given model and the observed distribution itself.

(e.g., Volonteri et al. 2007). In this process, there are two large uncertainties: the size of the warp radius and the direction of $\hat{\boldsymbol{J}}_{\rm CBHD}$. The size of the warp radius depends strongly on the ratio ν_2/ν_1 (Equation (6)). Many studies adopted $\nu_2/\nu_1 = 2(1+7\alpha^2)/[\alpha^2(4+\alpha^2)] \sim 85$, motivated by analyses of low-amplitude warps (Ogilvie 1999). On the other hand, Lodato & Gerosa (2013) have shown that when considering large-amplitude warps, ν_2/ν_1 is between ∼2 and 50 depending on $\alpha_{\rm SS}$ and the misalignment angle $\theta_{\rm BH,warp}$. We set ν_2/ν_1 to be a free parameter with a fiducial value of 10, and vary it from 2 to 50 (models M10 and M11).

For a single BH, $\hat{\boldsymbol{J}}_{\rm CBHD}$ aligns with $\hat{\boldsymbol{J}}_{\rm AGN}$ (see results in Lubow et al. 1999 in the context of protoplanetary disks). On the other hand, when a BH is in a binary, $\hat{\boldsymbol{J}}_{\rm CBHD}$ aligns with the orbital angular momentum direction of the binary $\hat{\boldsymbol{J}}_{\rm bin}$ on the disk's viscous timescale (e.g., Moody et al. 2019). Assuming a

Shakura–Sunyaev disk, the viscous timescale is given by

$$t_{\rm vis} \sim \frac{s^2}{\nu} \sim 10^2\ {\rm yr}\left(\frac{\alpha_{\rm SS}}{0.1}\right)^{-4/5}\left(\frac{\dot{m}_{\rm bin}}{\dot{m}_{\rm Edd,bin}}\right)^{-3/10} \times\left(\frac{m_{\rm bin}}{20\,M_\odot}\right)^{1/4}\left(\frac{s}{\rm au}\right)^{5/4}, \quad (8)$$

(e.g., Frank et al. 2002), where s is the binary separation, $m_{\rm bin}$ is the binary mass, $\dot{m}_{\rm bin}$ is the accretion rate onto the binary, $\dot{m}_{\rm Edd,bin} = L_{\rm Edd}/(\eta_{\rm c}c^2)$ is the Eddington accretion rate for the binary, and $\eta_{\rm c}$ is the radiative efficiency. Due to the short viscous timescale, in our fiducial setting we assume that $\hat{\boldsymbol{J}}_{\rm CBHD}$ is the same as $\hat{\boldsymbol{J}}_{\rm AGN}$ when a BH is single, and is the same as $\hat{\boldsymbol{J}}_{\rm bin}$ when a BH is in a binary. For comparison, we also investigate the alternative assumption that the direction of $\hat{\boldsymbol{J}}_{\rm CBHD}$ is always aligned with $\hat{\boldsymbol{J}}_{\rm AGN}$ (model M12).

We set the BH accretion rate to the minimum of the Eddington accretion rate and the Bondi–Hoyle–Lyttleton rate (Equation (24) in Paper I) taking into account a reduction due to the shearing motion of the nearby disk gas (Equations (29)–(32) in Paper I). When BHs are in binaries, we apportion the total accretion between primary and secondary BHs following Duffell et al. (2019), which is updated from Paper I, in which we used earlier results from Farris et al. (2014).

2.2.3. Mergers

Following BBH mergers, the dimensionless spin parameter $\boldsymbol{a}_{\rm f}$ of the remnant BH depends on the spins $\boldsymbol{a}_1$ and $\boldsymbol{a}_2$ and the dimensionless orbital angular momentum parameter $\boldsymbol{l}$ of the two original binary components.[7] We adopt the formula obtained from numerical simulations of BBH mergers in Rezzolla et al. (2008),

$$\boldsymbol{a}^{\rm f} = \frac{1}{(1+q)^2}(\boldsymbol{a}_1 + \boldsymbol{a}_2 q^2 + \boldsymbol{l}q), \quad (9)$$

where $q \equiv m_2/m_1 \leqslant 1$ is the mass ratio. The magnitude of $\boldsymbol{l}$ is given by

$$|\boldsymbol{l}| = \frac{s_4}{(1+q^2)^2}(|\boldsymbol{a}_1|^2 + |\boldsymbol{a}_2|^2 q^4 + 2|\boldsymbol{a}_1||\boldsymbol{a}_2|q^2\cos\theta_{12}) + \left(\frac{s_5\eta + t_0 + 2}{1+q^2}\right)(|\boldsymbol{a}_1|\cos\theta_{1b} + |\boldsymbol{a}_2|q^2\cos\theta_{2b}) + 2\sqrt{3} + t_2\eta + t_3\eta^2 \quad (10)$$

where $\eta \equiv q/(q+1)^2$ is the symmetric mass ratio, $s_4 = -0.129$, $s_5 = -0.384$, $t_0 = -2.686$, $t_2 = -3.454$, and $t_3 = 2.353$ are values obtained in Rezzolla et al. (2008), and θ_{12}, θ_{1b}, and θ_{2b} are the angles between the spins of the two BHs and their orbital angular momentum,

$$\cos\theta_{12} = \frac{\boldsymbol{a}_1\cdot\boldsymbol{a}_2}{|\boldsymbol{a}_1||\boldsymbol{a}_2|}, \quad (11)$$

$$\cos\theta_{1b} = \frac{\boldsymbol{a}_1\cdot\boldsymbol{l}}{|\boldsymbol{a}_1||\boldsymbol{l}|}, \quad (12)$$

$$\cos\theta_{2b} = \frac{\boldsymbol{a}_2\cdot\boldsymbol{l}}{|\boldsymbol{a}_2||\boldsymbol{l}|}. \quad (13)$$

According to Equation (9), if $a_1 = a_2 = 0$, $a^{\rm f}$ monotonically increases from 0.58 to 0.69 as q increases from 0.4 to 1 and decreases to 0 as $q \to 0$.

Following Rezzolla et al. (2008) and Dubois et al. (2014), we assume that GW radiation does not affect the direction of the orbital angular momentum, and set the direction of $\boldsymbol{l}$ to the binary orbital angular momentum at merger. Although Barausse & Rezzolla (2009) suggested that GW radiation modifies the binary orbital angular momentum direction just before merger, we neglect this correction for simplicity because results are not sensitive to the precise $\boldsymbol{a}^f$ direction. Similarly, we assume that $\chi_{\rm eff}$ values are unaffected by relativistic effects. This is justified if the BH spin directions and the orbital angular momentum directions are not influenced by the effects before binaries enter the frequency above which the LIGO/Virgo detectors are sensitive, which is $\sim$10 Hz. The orbital angular momentum direction is not directly influenced by the reaction to GW radiation significantly for circular orbits at lower frequencies (Barausse & Rezzolla 2009). The BH spin directions can be systematically affected by spin–orbit resonances due to precession of the BH spins, which can align or anti-align the BH spins with each other or cause nutation (Kesden et al. 2010; Gerosa et al. 2019). In our simulations, such resonances or nutation occur only within the detectable frequency band above 10 Hz for $\gtrsim$95% of stellar BH mergers. Thus, we conclude that these general relativistic effects have a small impact on the detectable $\chi_{\rm eff}$ distribution for LIGO/VIRGO.

2.3. Evolution of Binary Orbital Angular Momentum Direction

2.3.1. Initial Orbital Angular Momentum Direction

We consider four types of BH binaries distinguished by their formation process: (i) pre-existing binaries, (ii) gas-capture binaries, (iii) dynamically formed binaries, and (iv) remnants of stellar binaries formed in situ. For binaries belonging to (iii) we set $\hat{\boldsymbol{J}}_{\rm bin} = \pm\hat{\boldsymbol{J}}_{\rm AGN}$, and the ratio of aligned binaries to anti-aligned binaries to 1, as suggested by simulations of binary formation in migration traps (Secunda et al. 2020). For binaries belonging to (iv), we also set the ratio to be 1 for simplicity, although we note that this ratio is highly uncertain. On the other hand, for binaries belonging to (i) or (ii), the orbital angular momentum directions are presumed to be random. For simplicity, we assume that all binaries have zero eccentricity. We expect that this assumption does not significantly change the evolution of binary orbital angular momenta or BH spins.

As we show below, the initial angular momentum directions of binaries have a relatively small effect on the $\chi_{\rm eff}$ distribution measured at merger, because these directions are frequently randomized by binary–single interactions.

2.3.2. Gas Accretion

The orbital angular momentum directions of binaries evolve due to accretion torques. If the circumbinary gas is rotating in the same direction as the AGN disk, the binaries are aligned with the AGN disk since the relative velocity between the binary components and the gas is reduced by the accretion. Referring to Lubow et al. (1999), we assume that the angular

[7] $(G/c)m_1m_2\boldsymbol{l}$ is the orbital angular momentum at the ISCO.

momentum direction of the captured gas with respect to the binary ($\hat{\boldsymbol{J}}_{\rm gas}$) is the same as the angular momentum direction of the AGN disk with respect to the SMBH ($\hat{\boldsymbol{J}}_{\rm AGN}$) for binaries embedded in the AGN disk. The angular momentum of the captured gas is added to the binary orbital angular momentum as $\boldsymbol{J}_{\rm bin}^{\rm f} = \boldsymbol{J}_{\rm bin} + \boldsymbol{J}_{\rm gas}$, where we set

$$\boldsymbol{J}_{\rm gas} = f_{\rm rot} s v_{\rm bin}(s) \dot{m}_{\rm BHL} \Delta t \hat{\boldsymbol{J}}_{\rm AGN}, \tag{14}$$

and where $v_{\rm bin}(s) = \sqrt{Gm_{\rm bin}/s}$ is the relative rotation velocity of binary components, and $f_{\rm rot}$ is a parameter determining the efficiency of the alignment of the binary angular momentum direction due to gas capture. In the fiducial model, we set $f_{\rm rot} = 1$ assuming that the binary receives a torque from gas circularly rotating at $\sim s$ from the binary. However, a low degree of rotation ($f_{\rm rot} \sim 0$) of gas accreting onto a low-mass object in an AGN disk is suggested in simulations by Baruteau et al. (2011) and Derdzinski et al. (2019). For completeness, we investigate this case, as well as an opposite extreme case with $f_{\rm rot} = 10$ (models M13 and M14). Note that during gas accretion, the binary separation also evolves due to type I/II torque of the circumbinary disk (Paper I).

2.3.3. Binary–Single Interaction

After a hard binary–single interaction, the orbital angular momenta of binaries are modified due to chaotic interactions. In this paper, we simply assume that after a hard binary–single interaction, the orbital angular momentum direction of a binary becomes isotropically random.

Whenever a binary–single interaction occurs in the simulation, we choose a nearby third object, and assign a recoil kick velocity to it. If this third object is itself a binary, we assume that the softer binary is disrupted, while the harder binary experiences a hard binary–single interaction by regarding the softer binary as a single object for simplicity, and we assign the recoil kick velocity to its center of mass.

2.4. Merger Prescription

Since we track the evolution of the BH spins and the binary orbital angular momenta, we can estimate the recoil velocity due to anisotropic GW radiation and mass loss at mergers more precisely. We add the following prescriptions to the model used in Paper I.

2.4.1. Recoil Velocity at Merger

Due to the burst of anisotropic GW radiation at merger, a remnant BH receives a recoil kick. To calculate the recoil velocities, we adopt the fitting formulae obtained from numerical simulations by Lousto et al. (2012),

$$\begin{aligned}
\boldsymbol{v}_{\rm GW} &= v_{\rm m}\hat{\boldsymbol{e}}_x + v_\perp(\cos\xi\hat{\boldsymbol{e}}_x + \sin\xi\hat{\boldsymbol{e}}_y) + v_\parallel\hat{\boldsymbol{e}}_z,\\
v_{\rm m} &= A\eta^2\sqrt{1-4\eta}(1+B\eta),\\
v_\perp &= H\frac{\eta^2}{(1+q)}(a_2^\parallel - qa_1^\parallel),\\
v_\parallel &= \frac{16\eta^2}{1+q}[V_{1,1} + V_A\tilde{S}_\parallel + V_B\tilde{S}_\parallel^2 + V_C\tilde{S}_\parallel^3]\\
&\quad\times|a_1^\perp - qa_2^\perp|\cos(\phi_\Delta - \phi_1),
\end{aligned} \tag{15}$$

where $v_{\rm m}$ is a mass-asymmetry contribution, $v_\perp$ and $v_\parallel$ are kick components perpendicular and parallel to the orbital angular momentum, respectively,

$$\tilde{\boldsymbol{S}} \equiv 2\frac{\boldsymbol{a}_1 + q^2\boldsymbol{a}_2}{(1+q)^2}, \tag{16}$$

$\hat{\boldsymbol{e}}_x$, $\hat{\boldsymbol{e}}_y$ are orthogonal unit vectors in the orbital plane, and $\hat{\boldsymbol{e}}_z$ is the direction of the binary orbital angular momentum. The symbols $\parallel$ and $\perp$ refer to the directions parallel and perpendicular to the orbital angular momentum, respectively, and the numerical constants are $A = 1.2\times10^4\,{\rm km\,s^{-1}}$, $B = -0.93$, $H = 6.9\times10^3\,{\rm km\,s^{-1}}$, $\xi = 145^\circ \pm 5^\circ$, $V_{1,1} = 3678\,{\rm km\,s^{-1}}$, $V_A = 2481\,{\rm km\,s^{-1}}$, $V_B = 1792\,{\rm km\,s^{-1}}$, and $V_C = 1507\,{\rm km\,s^{-1}}$, ϕ_1 is the phase angle of the binary, and ϕ_Δ is the angle between the in-plane component of the vector

$$\boldsymbol{\Delta} = m_{\rm bin}^2\frac{\boldsymbol{a}_1 - q\boldsymbol{a}_2}{1+q} \tag{17}$$

and the infall direction at merger. We choose $\phi_\Delta - \phi_1$ from a random distribution uniform in $[0, \pi]$.

2.4.2. Mass Loss at Merger

Some fraction of the BH mass is radiated away due to GW radiation. We adopt a simplified approximation for the remnant mass from Barausse et al. (2012),

$$\begin{aligned}
\frac{m_{\rm rem}}{m_{\rm bin}} &= 1 - \eta(1-4\eta)[1 - E_{\rm ISCO}(\tilde{a}_\parallel)]\\
&\quad - 16\eta^2[p_0 + 4p_1\tilde{a}_\parallel(\tilde{a}_\parallel + 1)],
\end{aligned} \tag{18}$$

where

$$\tilde{E}_{\rm ISCO}(\tilde{a}_\parallel) \equiv \left(1 - \frac{2}{3r_{\rm ISCO}(\tilde{a}_\parallel)}\right)^{1/2} \tag{19}$$

is the energy per unit mass of a particle with spin

$$\tilde{\boldsymbol{a}} = \frac{\boldsymbol{a}_1 + q^2\boldsymbol{a}_2}{(1+q)^2}, \tag{20}$$

and $p_0 = 0.04827$ and $p_1 = 0.01707$ are parameters obtained by fitting numerical results.

2.4.3. Merger Condition

We assume that a binary merges when its separation s becomes smaller than the ISCO of a particle with mass $m_{\rm bin}$ and spin given in Equation (20). We subsequently treat the object as a single BH with a mass given by Equation (18).

2.5. Numerical Choices

Table 1 lists the parameter values adopted in the fiducial model (the same as Model 1 in Paper I). We assume that stars are distributed spherically with a Maxwell–Boltzmann velocity distribution, the stellar mass within 3 pc is $M_{\rm star,3pc} = 10^7\,M_\odot$, and the power-law slope of the stellar IMF is $\delta_{\rm IMF} = 2.35$. BHs are initially distributed from $r_{\rm in,BH} = 2\times10^{-4}\,{\rm pc}$ to $r_{\rm out,BH} = 3\,{\rm pc}$ with a cumulative radial profile

$$\frac{dN_{\rm BH,ini}(r)}{dr} \propto r^{\gamma_\rho} \tag{21}$$

with a power-law index $\gamma_\rho = 0$, where $N_{\rm BH,ini}(r)$ labels the total initial number of BHs within a distance r from the central SMBH.

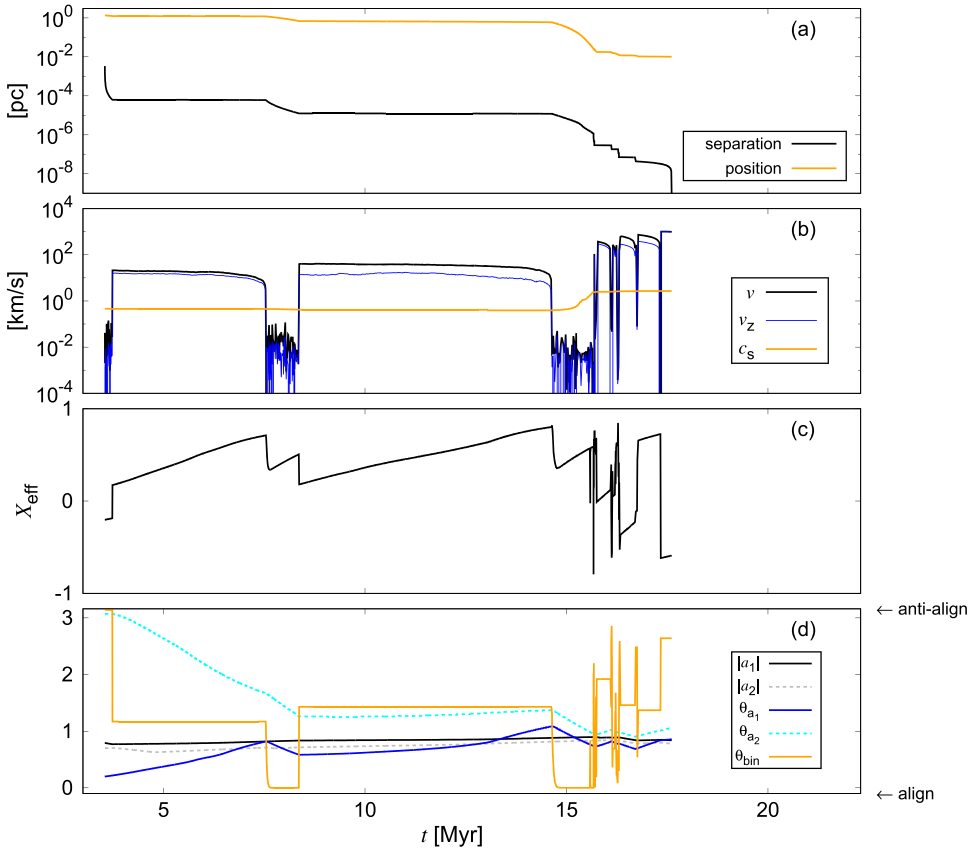

Figure 1. Evolution of several quantities for a binary in model M6 (in which $a_0 = 0.7$) formed via the gas-capture mechanism. (a) Binary separation (black) and distance from the SMBH (orange). (b) Velocity of the center of mass of the binary relative to the local motion of the AGN disk v (black), z-direction velocity v_z (blue), and sonic velocity of gas near the binary c_s (orange). While $v_z \leqslant c_s$, the typical height of orbital motion for the binary is less than the scale height of the AGN disk, which means that the binary is embedded in the AGN disk. (c) The effective spin parameter $\chi_{\rm eff}$. (d) Spin magnitude of binary components ($|a_1|$ and $|a_2|$, black and dashed gray), the angle between the BH spins $\hat{\boldsymbol{a}}_1$ or $\hat{\boldsymbol{a}}_2$ and the AGN angular momentum direction $\hat{\boldsymbol{J}}_{\rm AGN}$ (blue and dashed cyan), and the angle between the binary angular momentum direction $\hat{\boldsymbol{J}}_{\rm bin}$ and $\hat{\boldsymbol{J}}_{\rm AGN}$ (orange).

Note that BHs are assumed to have a flattened axisymmetric distribution (see Paper I). The x, y, and z velocities for BHs relative to the local Keplerian value $v_{\rm Kep}(r)$ are initially drawn from a Gaussian distribution with the dispersion of $\beta_{\rm v} v_{\rm Kep}(r)/\sqrt{3}$, where $\beta_{\rm v}$ is a velocity anisotropy parameter set to $\beta_{\rm v} = 0.2$ motivated by vector resonant relaxation (Szolgyen & Kocsis 2018). The total number and mass in BHs are calculated from the stellar mass, the stellar IMF, and the relation between the stellar and BH mass derived in Belczynski et al. (2010). We set the fraction of pre-existing binaries to be $f_{\rm pre} = 0.15$. In the fiducial model, there are initially 2×10^4 BHs and 1.5×10^3 binaries. As in Paper I, the time-step parameter is $\eta_t = 0.1$, and the number of radial cells storing physical quantities is $N_{\rm cell} = 120$.

The mass of the central SMBH is $M_{\rm SMBH} = 4 \times 10^6\, M_\odot$, the gas accretion rate from the outer radius is $\dot{M}_{\rm out} = 0.1 \dot{M}_{\rm Edd}$, where $\dot{M}_{\rm Edd} = L_{\rm Edd}/(\eta_{\rm c} c^2)$ is the Eddington accretion rate, here defined including a radiative efficiency of $\eta_{\rm c} = 0.1$. The efficiency of angular momentum transport in the α-disk is $\alpha_{\rm SS} = 0.1$ (Shakura & Sunyaev 1973) and the angular momentum transfer parameter is $m_{\rm AM} = 0.15$ (Thompson et al. 2005).

3. Results

3.1. $\chi_{\rm eff}$ Evolution: An Illustrative Example

We used the combination of semi-analytical calculations and simulations, described above, to investigate the $\chi_{\rm eff}$ distribution of BHs merging in AGN disks. An illustrative example of the evolution of such a BH binary is shown in Figure 1.

The binary in this figure forms via the gas-capture mechanism at $t = 3.5$ Myr at a distance of 1.3 pc from the SMBH, with an initial separation of 3.4×10^{-3} pc. The masses of the binary components are 10.7 and 6.8 $M_\odot$, the magnitudes of BH spins are 0.79 and 0.70, and the angles between the BH spins and $\hat{\boldsymbol{J}}_{\rm AGN}$ are 0.20 and 3.1 radians, respectively.[8] The separation of the binary (black line in panel (a)) decreases, successively, due to gas dynamical friction, binary–single interactions, and GW radiation as shown in Paper I. Although a binary is disrupted when its separation exceeds the Hill radius, ionization is extremely rare (≈1% of the number of mergers) due to rapid hardening by gas dynamical friction in early phases (see Figures 5 and 6 of Paper I).

While the binary is in the AGN disk ($v_z < c_s$, blue and orange lines in panel (b)), $\hat{\boldsymbol{J}}_{\rm bin}$ aligns with $\hat{\boldsymbol{J}}_{\rm AGN}$ due to accretion torque (orange line in panel (d)). Also, $\hat{\boldsymbol{a}}_1$ and $\hat{\boldsymbol{a}}_2$ (blue and cyan lines in panel (d)) evolve toward the angular momentum direction of a circum-BH disk, which is set to be the same as $\hat{\boldsymbol{J}}_{\rm bin}$. Such alignment of $\hat{\boldsymbol{a}}_1$ and $\hat{\boldsymbol{a}}_2$ with $\hat{\boldsymbol{J}}_{\rm bin}$ increases $\chi_{\rm eff}$ (panel (c)). The spin magnitudes, $|a_1|$ and $|a_2|$, evolve due to gas accretion (black and gray lines in panel (d)), but only by 20%

[8] At birth the initial value of both BH spins is 0.7 and the BH masses are 10.0 and 6.8 $M_\odot$, but the mass and spin of one of the BHs evolved due to gas accretion prior to binary formation.

and 11%, which are much smaller than the change in $\chi_{\rm eff}$. Until $t \sim 5$ Myr, $|a_2|$ slightly decreases as gas accretes since the anti-alignment condition (Equation (7)) is satisfied for the secondary BH.

After each binary–single interaction, $\hat{\boldsymbol{J}}_{\rm bin}$ is randomized, which reduces $|\chi_{\rm eff}|$ on average. Binary–single interactions become very frequent at $\lesssim$0.01 pc due to the high BH density, and binaries merging in the inner regions typically have experienced a larger number ($\approx$8) of binary–single interactions. Note that kicked BHs in the inner regions are typically easily recaptured, e.g., within $\sim$0.1 Myr at $r \sim 0.01$ pc for the kick velocity of $\sim$300 km s^{-1} (see Equation (26) and Figure 10 in Paper I). This binary merges outside the AGN disk 17.6 Myr after it formed, and its components accrete 2.0 and 1.7 $M_\odot$ until their merger. Since $\hat{\boldsymbol{a}}_1$ and $\hat{\boldsymbol{a}}_2$ are roughly anti-aligned with $\hat{\boldsymbol{J}}_{\rm bin}$ following binary–single interactions, $\chi_{\rm eff}$ at merger has a negative value of -0.59. Thus, $\chi_{\rm eff}$ in this case evolves through both gas accretion and binary–single interactions.

3.2. $\chi_{\rm eff}$ Distribution in Different Models

In this section, we present the probability distribution of $\chi_{\rm eff}$ as well as of several different quantities at the time of merger, obtained in our models. Because of the flexibility of our model, we are also able to study the dependence of these results on the choice of prescriptions and parameter values. In Table 2, we list the model variations we have investigated. These include the fiducial model (M1), and 23 different variations (models M2–M24). The variations can be divided into four categories. First, we examine different choices of the initial BH spin magnitudes and directions (models M2–M9). Second, we vary the prescriptions for the evolution of the BH spin directions and the binary angular momentum directions during gas accretion (models M10–M14). Third, we study different parameters related to the AGN disk (models M15–M19). Finally, we vary the properties of the initial BH population (models M20–M24).

Figure 2 shows our main results, namely the differential probability distributions of $\chi_{\rm eff}$, $|\boldsymbol{a}|$, $\cos\theta_a$, $\cos\theta_{\rm bin}$, and $m_{\rm chirp}$ (first to fifth column, respectively). Here, $|\boldsymbol{a}|$ stands for either $|\boldsymbol{a}_1|$ or $|\boldsymbol{a}_2|$, and θ_a and $\theta_{\rm bin}$ are the angles between ($\hat{\boldsymbol{a}}$) and the binary orbit ($\hat{\boldsymbol{J}}_{\rm bin}$) with respect to the AGN disk ($\hat{\boldsymbol{J}}_{\rm AGN}$). The four different rows in this figure correspond to the four different types of model variations, as discussed above and labeled in the figure.

The distributions of all predicted quantities in Figure 2 are weighted by the detectable volume, which enables us to compare our predictions to the observed distribution (dashed red lines). The detectable volume is calculated via Equation (6) of The LIGO Scientific Collaboration and The Virgo Collaboration (2012) and using the noise spectral density of the ER13 (prior to O3) run of LIGO Hanford (Kissel & Betzwieser 2018), in which the volume is assumed to depend only on the masses of the binary components. The volume is roughly proportional to $m_1^{2.2}$ for $m_{\rm bin} \lesssim 100\,M_\odot$ (e.g., Fishbach & Holz 2017). Furthermore, to compare with the observed distributions of $\chi_{\rm eff}$ and $m_{\rm chirp}$, we add observational errors to $\chi_{\rm eff}$ and $m_{\rm chirp}$ for each merger in the simulations.[9] For a simple treatment, we draw the errors of $\chi_{\rm eff}$ and $m_{\rm chirp}$ from independent Gaussian distributions whose 90% intervals are ±0.2 and $\pm0.08 m_{\rm chirp}$, respectively, which match the typical O1/O2 observational error magnitudes (The LIGO Scientific Collaboration et al. 2019). These errors are added to our predictions for the analysis of the Kolmogorov–Smirnov (KS) test and Figures 2–9 below (see Figure 10 for results without errors).

In Figure 3 we present the cumulative probability distributions, rather than the differential ones shown in Figure 2. We present and discuss results at $t = 10$ Myr unless stated otherwise (but see Table 2 for different choices).

The fiducial model is shown by black lines in all of the panels, (a)–(e), of Figures 2 and 3. Panel (d) shows that $\theta_{\rm bin}$ represents an isotropic distribution (uniform in $\cos\theta_{\rm bin}$). This is because $\hat{\boldsymbol{J}}_{\rm bin}$ is frequently randomized by binary–single interactions. On the other hand, $\hat{\boldsymbol{a}}_1$ and $\hat{\boldsymbol{a}}_2$ tend to align with $\hat{\boldsymbol{J}}_{\rm AGN}$ (small θ_a) for the following reason. First, $\hat{\boldsymbol{a}}_1$ and $\hat{\boldsymbol{a}}_2$ are gradually aligned with $\hat{\boldsymbol{J}}_{\rm bin}$ due to gas accretion. However, $\hat{\boldsymbol{J}}_{\rm bin}$ aligns with $\hat{\boldsymbol{J}}_{\rm AGN}$ when the binary is in the AGN disk and it is mostly random when outside of it. Thus, the θ_a distribution is influenced by the fraction of the time that binaries typically spend in the AGN disk.

The mean spin magnitude $|\boldsymbol{a}|$ evolves from 0 in the fiducial model to typically lie in the range 0.08–0.64, $\chi_{\rm eff}$ and $m_{\rm chirp}$ are typically in the range -0.22 to $+0.24$ (-0.18 to $+0.21$ if no errors are added) and 8–49 $M_\odot$, respectively (enclosing 68% of the total probability). By comparison, for first-generation[10] mergers $|\boldsymbol{a}|$, $\chi_{\rm eff}$, and $m_{\rm chirp}$ are distributed in the ranges 0.044–0.32, -0.15 to $+0.20$, and 7–11 $M_\odot$, respectively. The median radial position r for first-generation mergers is 0.012 pc, while that for higher-generation mergers is 0.0098 pc. The weak dependence of the merger location on the generation occurs because gaps form around BHs at $r \sim 0.01$ pc, which significantly slows down the migration of BHs. Also, at $t = 0.1$ and 1 Myr, $m_{\rm chirp}$ is distributed over the ranges 6–11 $M_\odot$ and 7–15 $M_\odot$, respectively, and $|\boldsymbol{a}|$ is distributed over the ranges 0.002–0.005 and 0.009–0.60. The spin magnitude $|\boldsymbol{a}|$ goes to $\sim$0.6 when the disk is allowed to be present for 1 Myr, because second-generation mergers start between 0.1 and 1 Myr (and for $<$0.1 Myr, $|\boldsymbol{a}|$ remains close to 0). Hence, $|\boldsymbol{a}|$ and $m_{\rm chirp}$ both evolve significantly due to mergers. This trend is also visible in Figure 11, which shows that the standard deviation of $\chi_{\rm eff}$ increases with $m_{\rm chirp}$ (orange line in panel (a)). It is notable that a similar trend is also seen in the observed distribution (orange line in panel (t)).

To see the robustness of this trend, in Figure 5 we plot the weighted mean and standard deviation of $\chi_{\rm eff}$ as a function of mass for 10 additional simulations for independent realizations of the initial condition. The orange line in Figure 5 shows the standard deviation averaged over 11 runs. Here, the weighted standard deviation of quantity x_i for each model is calculated as

$$s_j = \left(\frac{M_j}{M_j - 1} \sum_{i \in j} w_i (x_i - \bar{x}_j)^2 \Big/ \sum_{i \in j} w_i \right)^{1/2} \tag{22}$$

where i is the index of a merger, w_i is the detectable volume, j is the index of a bin, M_j is the number of nonzero weights, and $\bar{x}_j = \sum_{i \in j} w_i x_i \big/ \sum_{i \in j} w_i$ is the weighted mean of x_i in the jth bin. In Figure 5, the errors of the mean and the standard deviation

[9] We note that $|a_1|$, $|a_2|$, $\cos\theta_{a1}$, $\cos\theta_{a2}$ have very large observational uncertainties; these quantities are currently not measurable independently from GW data. We show the predicted distributions without observational errors for these parameters.

[10] Mergers among BHs that did not merge earlier.

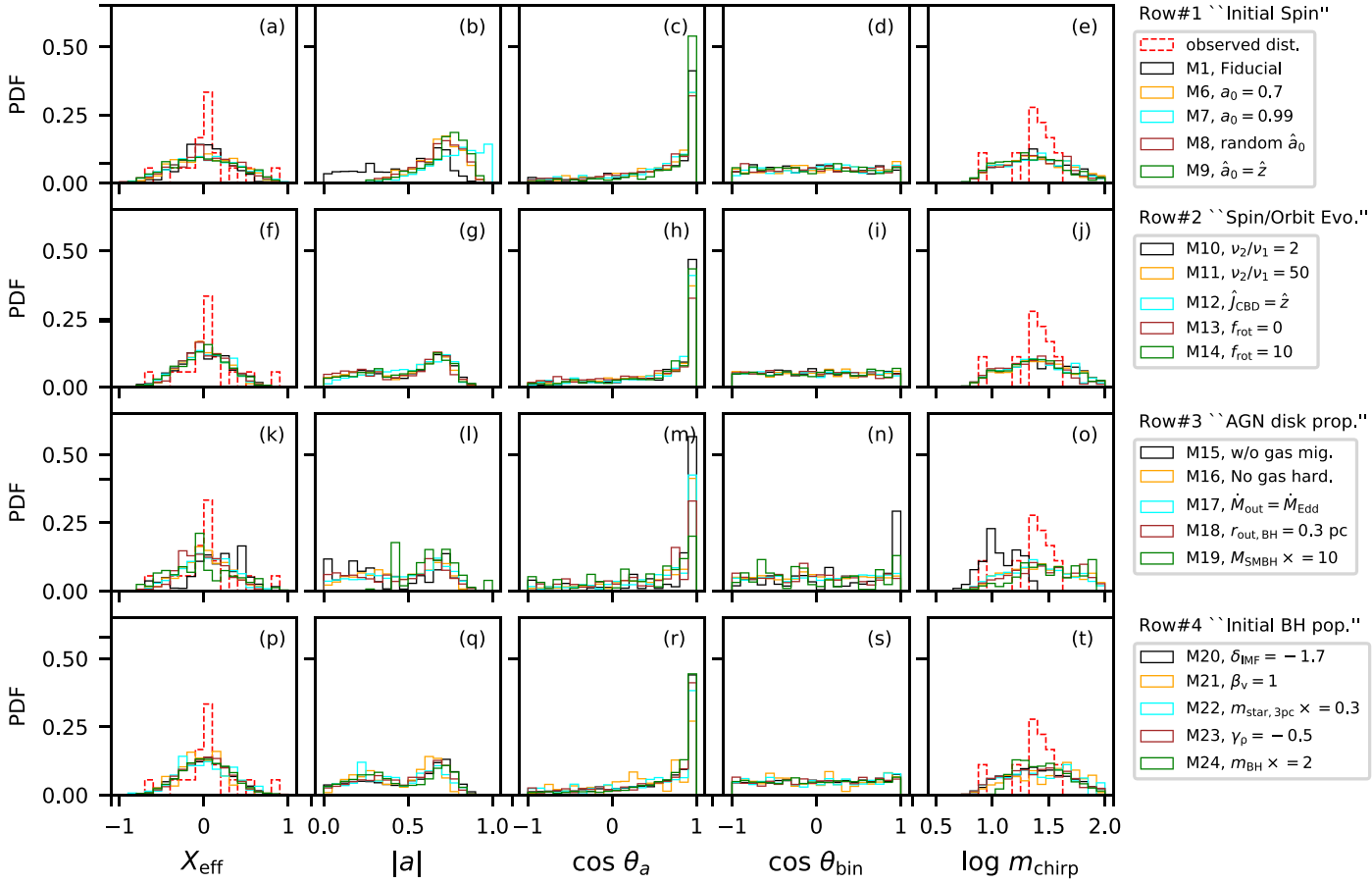

Figure 2. The probability distributions of $\chi_{\rm eff}$, a, $\cos\theta_a$, $\cos\theta_{\rm bin}$, and $m_{\rm chirp}$ at the time of the merger (left to right columns). Dashed red lines in the leftmost and rightmost panels are the distributions inferred from the GW events observed by LIGO/Virgo (Table 3). All predicted distributions are weighted by the volume detectable by LIGO, and observational errors have been added to the predicted $\chi_{\rm eff}$ and $m_{\rm chirp}$ values (see text). The black lines in the first row correspond to the fiducial model (M1), and the other colors and the other three rows consider different variations of the model (M2–M24), as labeled on the right and listed in Table 2.

are calculated as

$$\sigma(\bar{x}_j) = \frac{s_j}{\sqrt{M_j}} \tag{23}$$

and

$$\sigma(s_j) = s_j \left(\frac{1}{2(M_j - 1)}\right)^{1/2}, \tag{24}$$

respectively (Harding et al. 2014). Equation (24) is approximately correct for $M_j \gtrsim 10$. Figure 5 shows that the standard deviation of $\chi_{\rm eff}$ robustly increases up to $m_{\rm chirp} \sim 20\,M_\odot$, while it is roughly constant in the range $20\,M_\odot \lesssim m_{\rm chirp} \lesssim 100\,M_\odot$.

Next, we present the dependence of the distributions on the assumed initial BH spins (first row in Figure 2). In models M1 and M7, the initial BH spins are set to $|a_0| = 0$ and 0.99, respectively. We also examined five intermediate cases, with $|a_0| = 0.1$, 0.2, 0.3, 0.5, and 0.7 (models M2–M6) and found that the resulting distributions for all five quantities lie in-between those of the extreme models M1 and M7. For clarity, the intermediate cases (M2–M5) are therefore not shown in Figures 2 and 3. Gas accretion typically does not cause a systematic shift, but rather smears the initial distribution of $|a|$ (dashed line in Figure 3(b)). It typically increases the spin parallel to the orbital angular momentum, which is frequently reoriented in random directions by binary–single interactions. In contrast, $|a|$ evolves to $\sim$0.7 after mergers (solid and dashed black and blue lines). Models M1 and M7 show that $|a_0|$ has an influence on the $|\boldsymbol{a}|$ and the $\chi_{\rm eff}$ distributions. This is seen as the difference between the black and the cyan lines in panels (a) and (b) in Figures 2 and 3. This suggests that the initial spin distribution might be constrained by GW observations if they originate in AGN disks.

To examine the effects of the initial spin directions, in model M8 we set $|a_0| = 0.7$ and draw random $\hat{\boldsymbol{a}}_0$ directions, and in model M9 we set $\boldsymbol{a}_0 = 0.7\hat{\boldsymbol{J}}_{\rm AGN}$ for all (i.e., including pre-existing) BHs. The resulting distributions for model M8 are similar to those in model M6 (orange and brown lines in the top row). This is because the difference between models M6 and M8 is only the initial spin directions for BHs formed in situ, whose contribution to all mergers is small ($\sim$1%). The alignment of $\boldsymbol{a}_0$ with $\hat{\boldsymbol{J}}_{\rm AGN}$ in model M9 might be realized if previous AGN episodes yield spin directions aligned with the present-day disk orientation. We include this extreme model as an academic exercise to investigate the impact of full initial spin alignment. In this model, M9, θ_a is distributed around low values due to the initial direction of $\boldsymbol{a}_0$, while M6 and M8 have broader distributions. The orange and green lines in panel (a) suggest that the $\boldsymbol{a}_0$ direction has a negligible influence on the $\chi_{\rm eff}$ distribution.

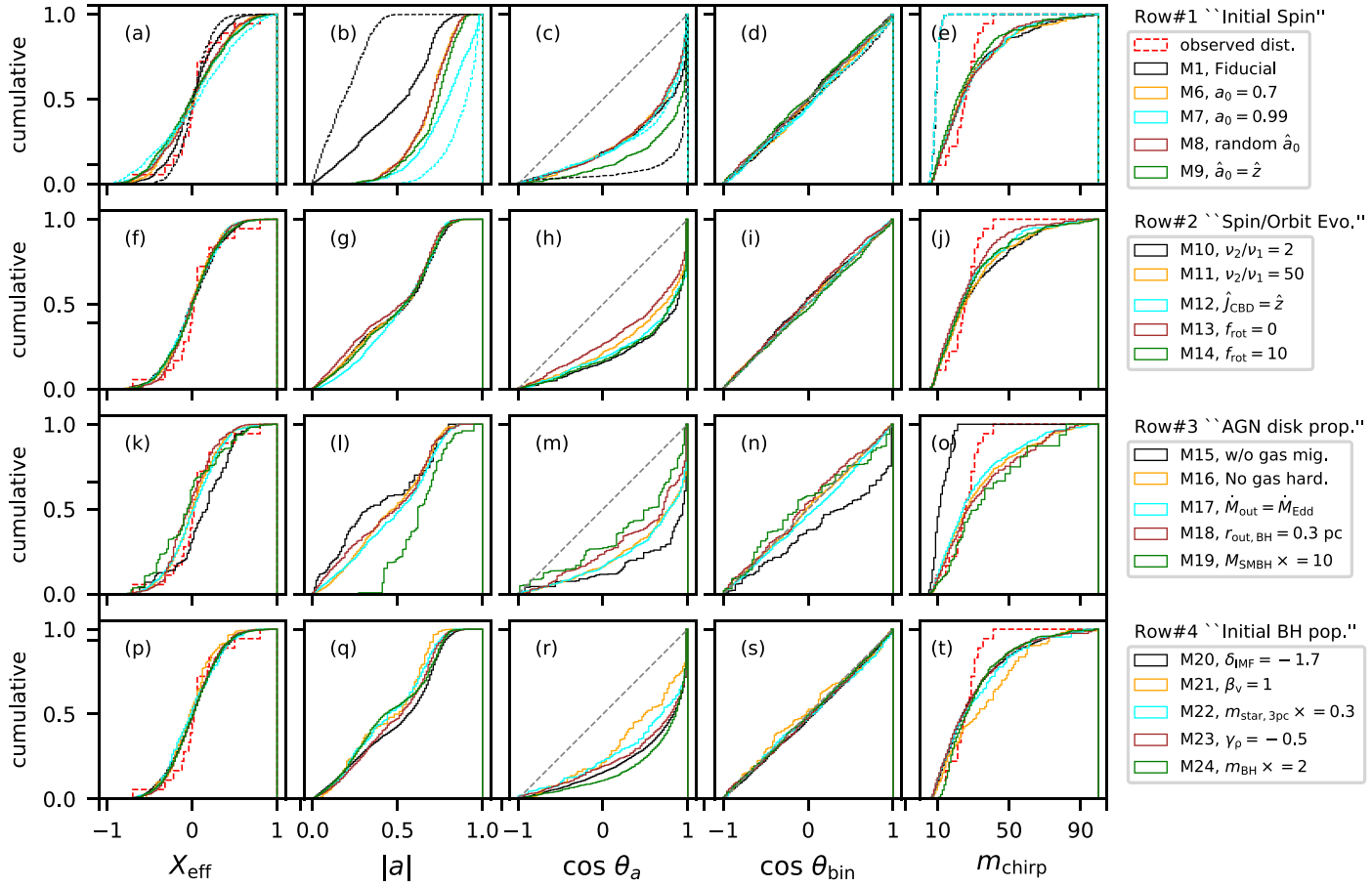

Figure 3. Same as Figure 2, but showing cumulative distributions. The dashed gray lines in the third and fourth columns represent isotropic distributions. In models M1 and M7, we present the distributions of first-generation mergers by dashed lines in panels (a)–(e).

Models M10–M14 (second row in Figures 2 and 3; panels (f)–(j)) show the results when changing the prescriptions or the parameters affecting the evolution of $\hat{\boldsymbol{a}}$ and $\hat{\boldsymbol{J}}_{\rm bin}$ during the accretion episodes. When the BH spins align efficiently due to enhanced viscosity accelerating the Bardeen–Petterson effect (model M11) or when the angular momentum of gas captured by the binaries is random (model M13), θ_a is slightly closer to an isotropic distribution (orange and brown lines in panel (h)). Nevertheless, we can see that these changes have a small impact on the $\chi_{\rm eff}$ distribution (panel (f)). This is simply because the timescale of randomization of $\hat{\boldsymbol{J}}_{\rm bin}$ due to binary–single interactions is shorter than the timescale of alignment of $\hat{\boldsymbol{a}}$ toward $\hat{\boldsymbol{J}}_{\rm bin}$ due to gas accretion. Likewise, these prescriptions have very little impact on the distribution of the other quantities.

In the third rows of Figures 2 and 3, we examine the impact of AGN disk properties. It is not clear whether (or to what extent) radial migration operates due to the complexity of the effects of N-body migrators (Broz et al. 2018), feedback from BHs (del Valle & Volonteri 2018; Regan et al. 2019), and inhomogeneities in the turbulent accretion disk (Laughlin et al. 2004; Baruteau & Lin 2010). In model M15 (shown in black lines), radial migration due to torques from the AGN disk is assumed to be inefficient. In this model, θ_a and $\theta_{\rm bin}$ (panels (m) and (n)) are distributed around lower values than those in the fiducial model. This is because binaries cannot migrate to regions of high BH density, where disorienting binary–single interactions are frequent (Paper I). As a result, $\chi_{\rm eff}$ is distributed toward higher values (panel (k)). Also, $m_{\rm chirp}$ tends to be lower since repeated "hierarchical" mergers, which build up the more massive BHs, are less frequent (panel (o)). We note here that, except for model M15, the $m_{\rm chirp}$ distributions are very similar in all model variants (panels (e), (j), (o), and (t)). This is because the $m_{\rm chirp}$ distributions are determined primarily by how often repeated mergers occur, and this is not significantly influenced by the parameters we changed, other than the efficiency of migration. On the other hand, the $\chi_{\rm eff}$ and $m_{\rm chirp}$ distributions for a model without migration would be sensitive to various other parameters, such as the initial mass distribution of BHs and the AGN lifetime.

In the bottom row of Figures 2 and 3, in models M16–M24, we examine the influence of the parameters of the AGN disk or the initial BH distribution (see Table 2). For example, in Model 18, we reduced the maximum radius at which BHs initially exist $r_{\rm out,BH}$, which is roughly equivalent to changing the size of the AGN disk. The resulting $\chi_{\rm eff}$ distributions are similar in these models (panels (k) and (p)). This is again because the $\chi_{\rm eff}$ distribution is mainly affected by how frequently spin-disorienting binary–single interactions take place, which is not sensitive to the changes mentioned above.

Overall, we find that the $\chi_{\rm eff}$ distribution is relatively sensitive to the values of $|a_0|$ and the efficiency of migration, and the $m_{\rm chirp}$ distribution is significantly influenced by

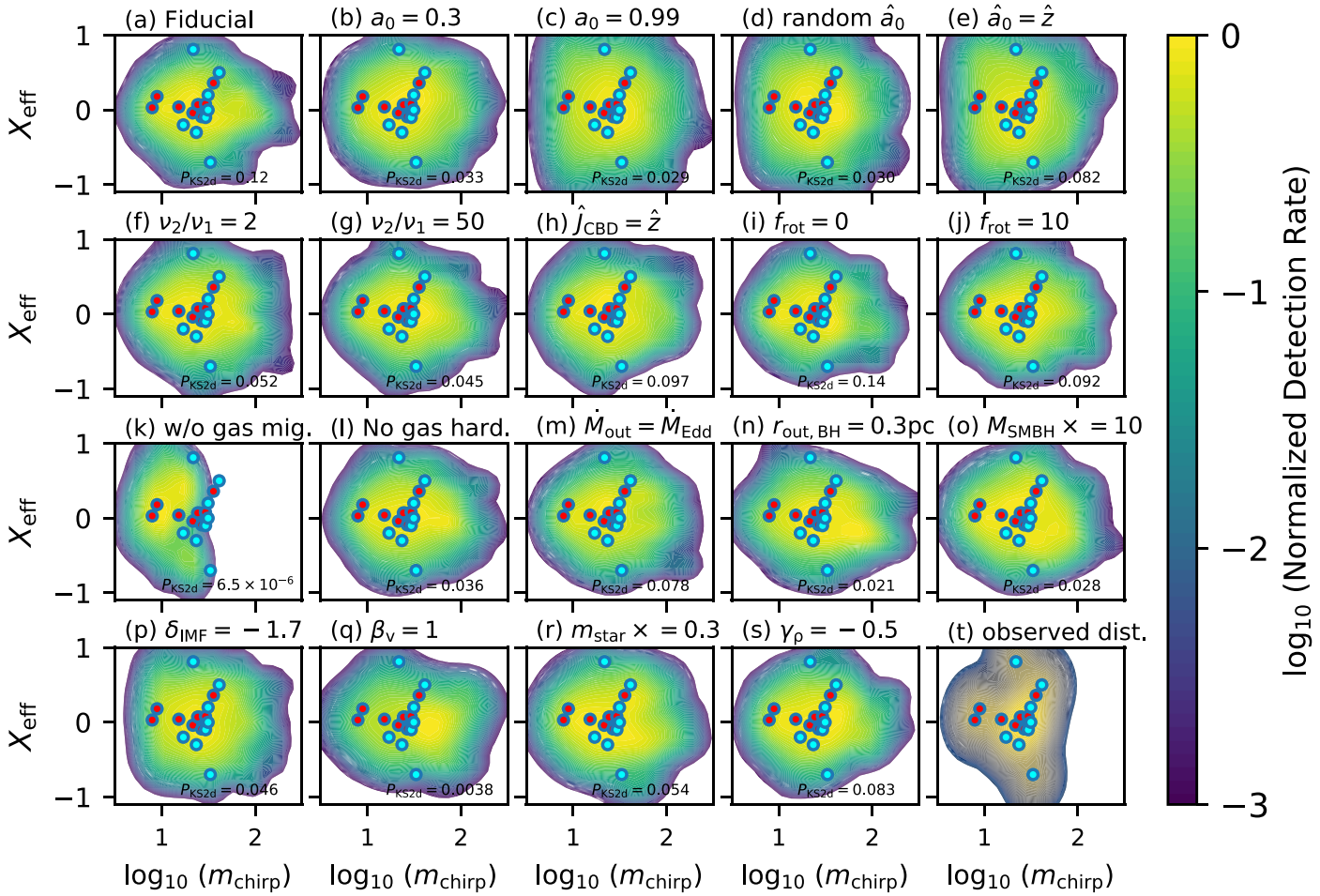

Figure 4. The normalized detection rate of mergers in the $m_{\rm chirp}$ vs. $\chi_{\rm eff}$ plane for several models. The detection rate is smoothed by performing a kernel-density estimate and normalized by the maximum value in each plane. Observational errors have been added to the predicted $\chi_{\rm eff}$ and $m_{\rm chirp}$ values. Panels (a)–(s) shows the detection rate distribution at 10 Myr for models M1, M4, M7–M23, respectively. The probability that the $\chi_{\rm eff}$ and $m_{\rm chirp}$ distributions for all events are reproduced by each model (the AGN contribution to all mergers is $f_{\rm AGN} = 1$) estimated by the KS test ($P_{\rm KS,\chi_{\rm eff},m_{\rm chirp}}$) is shown in the lower right corner. Panel (t) shows the distribution derived by performing a kernel-density estimate for the observed distribution, which is shown in different colors to emphasize its peculiarity. The values for the events inferred from the LIGO/Virgo collaboration (red circles) and the IAS group (cyan circles) are overplotted in all panels.

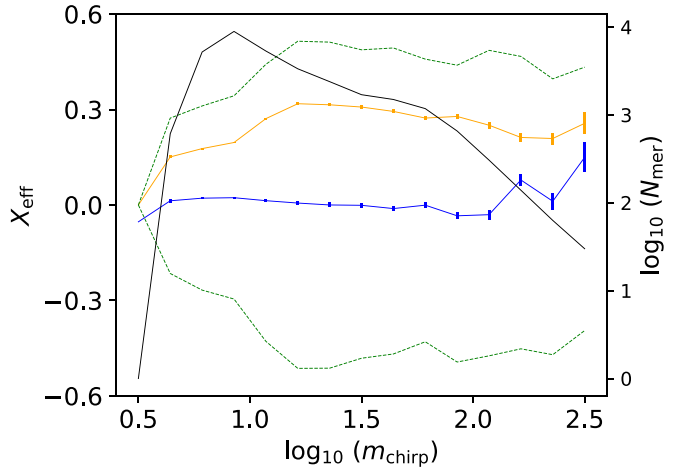

Figure 5. The average values and 1σ errors of the mean (cyan) and the standard deviation (orange) of $\chi_{\rm eff}$ as a function of $m_{\rm chirp}$ in 10 additional simulations of model M1 with independent realizations of the initial condition. Dashed green lines represent the 5th and 95th percentiles of $\chi_{\rm eff}$. The black line shows the number of mergers summed over 11 runs in mass bins of 0.133 dex (with corresponding values shown on the y-axis on the right).

migration. In the next section, we compare these predictions with observations.

3.3. Comparison with Observed Distribution

In Figures 6 and 7, we compare the $\chi_{\rm eff}$ distributions predicted by our models with that inferred from the observed GW events. In the observed distribution reported by the LIGO and Virgo collaborations (The LIGO Scientific Collaboration et al. 2019) the $\chi_{\rm eff}$ values are concentrated at low absolute values, near zero (Figure 7). On the other hand, a few possible additional events have been identified with higher and lower $\chi_{\rm eff}$ values (Figure 6, Venumadhav et al. 2019; Zackay et al. 2019, 2020; but see also Huang et al. 2020). Note that the IAS group (e.g., Zackay et al. 2019) and the Hannover group (Nitz et al. 2020) also recovered the events reported by the LIGO/Virgo collaborations.

In Figure 4, we additionally show the detection rate distributions predicted in several models in the $\chi_{\rm eff}$ versus $m_{\rm chirp}$ plane, together with the distribution inferred from the observed GW events (Table 3).

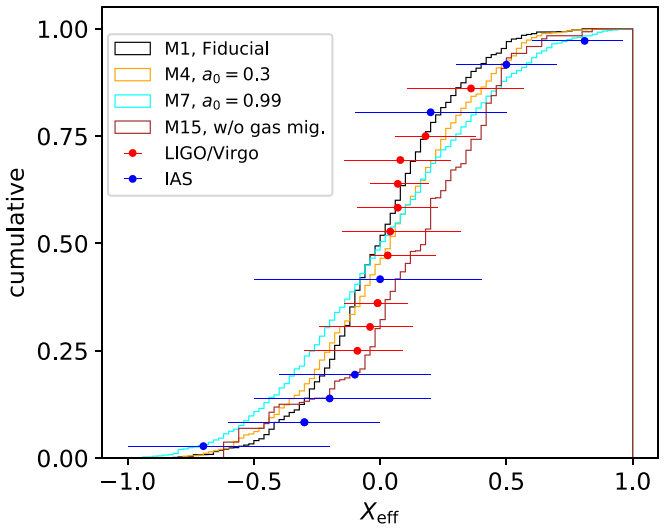

Figure 6. Comparison between the $\chi_{\rm eff}$ distribution inferred from the observed GW events and those predicted in our models. Black, orange, cyan, and brown lines show the distribution in models M1, M4, M7, and M15, respectively. The predicted distributions are weighted by the detectable volume and include observational errors. Red and blue circles show the median $\chi_{\rm eff}$ values reported by The LIGO Scientific Collaboration et al. (2019) and the IAS group (Venumadhav et al. 2019; Zackay et al. 2019, 2020), respectively. Error bars correspond to 90% credible intervals.

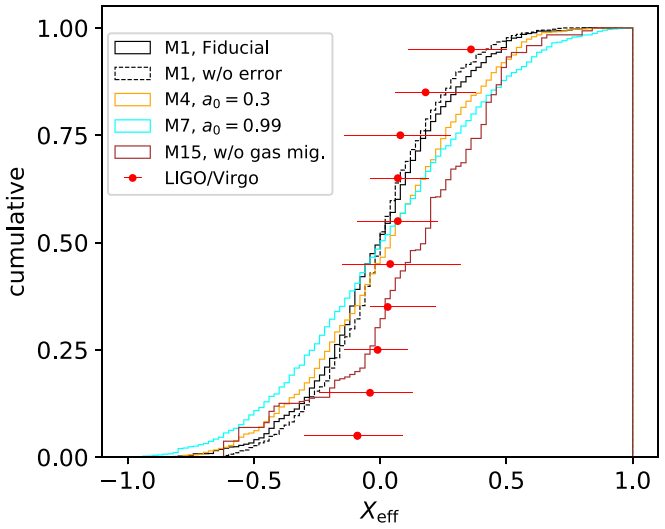

Figure 7. Same as Figure 6, but compared only with the events reported by the LIGO and Virgo collaborations (O1/O2). The distribution without errors is shown by the dashed line.

To compare the predicted and the observed distributions quantitatively, we use the KS test as well as a Bayesian analysis. The KS test enables us to estimate the probability that the distribution of all or a subset of the observed events is reproduced by a given model, while the Bayesian analysis can be used to assess how consistent each individual event is with a given model.

3.3.1. KS Test

Table 2 lists the results of the KS test. In each model, $P_{{\rm KS},\chi_{\rm eff}}$, $P_{{\rm KS},m_{\rm chirp}}$, and $P_{{\rm KS},\chi_{\rm eff},m_{\rm chirp}}$ are the probabilities that the set of all measured $\chi_{\rm eff}$ and $m_{\rm chirp}$ values were drawn from the one-dimensional $\chi_{\rm eff}$ and $m_{\rm chirp}$ distributions and the joint two-dimensional ($\chi_{\rm eff}$, $m_{\rm chirp}$) distributions predicted in that model,

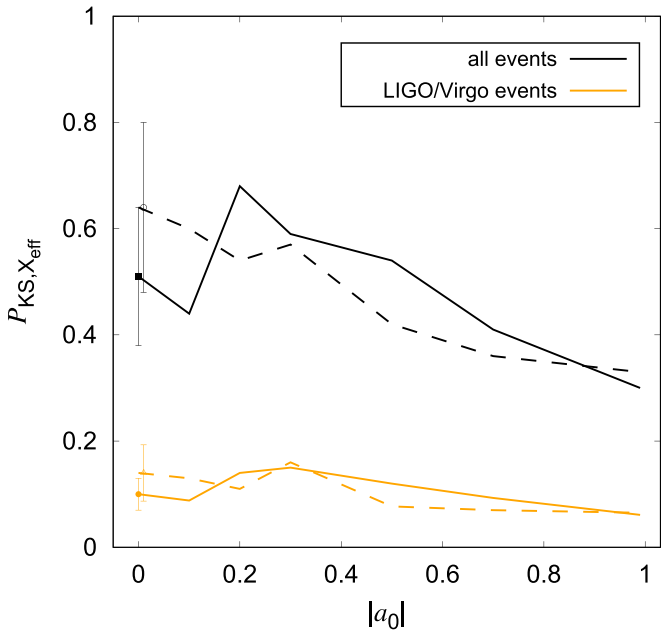

Figure 8. The KS probabilities that the one-dimensional $\chi_{\rm eff}$ distribution inferred from observed GW events are consistent with models assuming different initial spin magnitudes $|a_0|$ (i.e., models M1–M7). Black and orange lines show the results in which all observed GW events and only the LIGO/Virgo events are used, respectively. Solid and dashed lines show the results in which errors are and are not included in the predicted $\chi_{\rm eff}$ distribution, respectively. For $a_0 = 0$, the errors and means are calculated by performing 10 additional runs with different realizations of the initial conditions. The observed $\chi_{\rm eff}$ distribution slightly favors moderate values of $|a_0| \lesssim 0.5$.

computed following Press & Teukolsky (1988). $P_{{\rm KS,LV},\chi_{\rm eff}}$ and $P_{{\rm KS,LV},m_{\rm chirp}}$ are the probabilities that $\chi_{\rm eff}$ and $m_{\rm chirp}$ values for the events reported by the LIGO/Virgo collaborations were drawn from the predicted one-dimensional $\chi_{\rm eff}$ and $m_{\rm chirp}$ distributions, respectively. Figure 4 also lists $P_{{\rm KS},\chi_{\rm eff},m_{\rm chirp}}$ in each panel. As described in Figures 2 and 3, each predicted merger is weighted by the detectable volume, and errors are added to the predicted $\chi_{\rm eff}$ and $m_{\rm chirp}$ values.

The values of $P_{{\rm KS},\chi_{\rm eff},m_{\rm chirp}}$ are typically $\sim$0.01–0.1, except for model M15, which yields a much lower value of $P_{{\rm KS},\chi_{\rm eff},m_{\rm chirp}} = 6.5 \times 10^{-6}$. This is because $m_{\rm chirp}$ is typically much lower in model M15 than in the other models, as well as lower than the observations (panel (k) in Figure 4, $P_{{\rm KS},m_{\rm chirp}} = 9.2 \times 10^{-9}$). As explained above, this is because in this model (M15), radial migration is turned off; this makes hierarchical mergers much less common. We note, however, that the $m_{\rm chirp}$ distribution has large uncertainties in our models, for several reasons. First, we do not take into account the exchange of binary components during binary–single interactions, which affects the $m_{\rm chirp}$ distribution (the main assumptions in our models are listed in Section 2 of Paper I). Also, the time evolution of the AGN disk model, which we ignore, may affect the merged mass distribution (Section 5.7.1 of Paper I). Indeed, using an AGN lifetime of 30 Myr in Paper I, we found that the mass distribution of merging BHs extends to the values matching the observations if radial migration is turned off (see Figure 14(a) and (d) therein). Additional uncertainties include the stellar IMF in galactic centers (Lu et al. 2013) and the relation between the initial stellar mass and its remnant BH mass (e.g., Belczynski et al. 2010; Chen et al. 2015). Particularly, we neglected the possibility that BHs may be

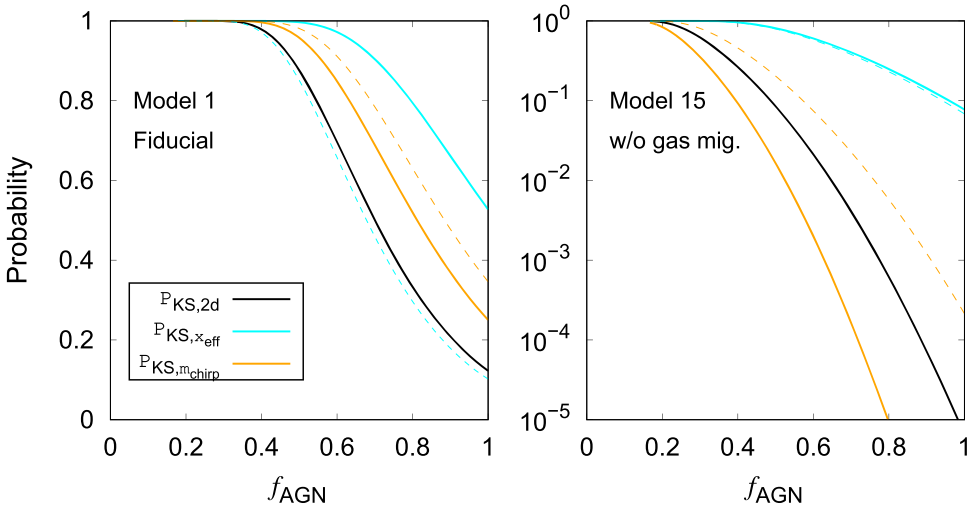

Figure 9. The KS probabilities that all events are produced by each model, as a function of the fraction of all mergers produced in AGN disks. Black, cyan, and orange lines show $P_{\rm KS,\chi_{eff},m_{chirp}}$, $P_{\rm KS,\chi_{eff}}$, and $P_{\rm KS,m_{chirp}}$, respectively. The left and right panels present results for the fiducial model M1 and the worst-fit model M15, respectively. Solid lines show the KS probabilities including all events claimed to date (Table 3), while dashed lines include only the LIGO/Virgo O1/O2 events (The LIGO Scientific Collaboration et al. 2019). The probabilities remain high ($\gtrsim$70%) in all cases, as long as the AGN channel is responsible for $\sim$30% or less of all events.

Table 3

The Data Sets Used in This Paper, Adopted from [1]: The LIGO Scientific Collaboration et al. (2019), [2]: Zackay et al. (2019), [3]: Venumadhav et al. (2019), and [4]: Zackay et al. (2020)

Event	$M_{\rm chirp}$	$M^{\rm det}_{\rm chirp}$	$\chi_{\rm eff}$	q	z	Reference	$K_{\rm M1,obs,\it i}$
GW150914	$28.6^{+1.6}_{-1.5}$	⋯	$-0.01^{+0.12}_{-0.13}$	$0.87^{+0.12}_{-0.21}$	$0.09^{+0.03}_{-0.03}$	[1]	0.29
GW151012	$15.2^{+2.0}_{-1.1}$	⋯	$0.04^{+0.28}_{-0.19}$	$0.59^{+0.36}_{-0.34}$	$0.21^{+0.09}_{-0.09}$	[1]	0.77
GW151226	$8.9^{+0.3}_{-0.3}$	⋯	$0.18^{+0.20}_{-0.12}$	$0.56^{+0.38}_{-0.33}$	$0.09^{+0.04}_{-0.04}$	[1]	0.88
GW170104	$21.5^{+2.1}_{-1.7}$	⋯	$-0.04^{+0.17}_{-0.20}$	$0.65^{+0.30}_{-0.22}$	$0.19^{+0.07}_{-0.08}$	[1]	0.51
GW170608	$7.9^{+0.2}_{-0.2}$	⋯	$0.03^{+0.19}_{-0.07}$	$0.70^{+0.27}_{-0.36}$	$0.07^{+0.02}_{-0.02}$	[1]	1.4
GW170729	$35.7^{+6.5}_{-4.7}$	⋯	$0.36^{+0.21}_{-0.25}$	$0.68^{+0.28}_{-0.28}$	$0.48^{+0.19}_{-0.20}$	[1]	0.23
GW170809	$25.0^{+2.1}_{-1.6}$	⋯	$0.07^{+0.16}_{-0.16}$	$0.67^{+0.29}_{-0.23}$	$0.20^{+0.05}_{-0.07}$	[1]	0.36
GW170814	$24.2^{+1.4}_{-1.1}$	⋯	$0.07^{+0.12}_{-0.11}$	$0.83^{+0.15}_{-0.23}$	$0.12^{+0.03}_{-0.04}$	[1]	0.44
GW170818	$26.7^{+2.1}_{-1.7}$	⋯	$-0.09^{+0.18}_{-0.21}$	$0.76^{+0.21}_{-0.24}$	$0.20^{+0.07}_{-0.07}$	[1]	0.30
GW170823	$29.3^{+4.2}_{-3.2}$	⋯	$0.08^{+0.20}_{-0.22}$	$0.76^{+0.22}_{-0.28}$	$0.34^{+0.13}_{-0.14}$	[1]	0.28
GW151216	22 ± 3	31^{+2}_{-3}	$0.81^{+0.15}_{-0.21}$	$0.7^{+0.3}_{-0.3}$	$0.43^{+0.17}_{-0.17}$	[2]	0.050
GW170121	23 ± 4	29^{+4}_{-3}	$0.3^{+0.3}_{-0.3}$	$0.76^{+0.19}_{-0.26}$	$0.24^{+0.14}_{-0.13}$	[3]	0.39
GW170304	31 ± 7	47^{+8}_{-7}	$0.2^{+0.3}_{-0.3}$	$0.75^{+0.19}_{-0.25}$	$0.5^{+0.2}_{-0.2}$	[3]	0.27
GW170727	29 ± 6	42^{+6}_{-6}	$-0.1^{+0.3}_{-0.3}$	$0.7^{+0.2}_{-0.3}$	$0.43^{+0.18}_{-0.17}$	[3]	0.30
GW170425	31 ± 15	47^{+26}_{-10}	$0.0^{+0.4}_{-0.5}$	$0.6^{+0.3}_{-0.3}$	$0.5^{+0.4}_{-0.3}$	[3]	0.44
GW170202	17 ± 3	$21.6^{+4.2}_{-1.4}$	$0.2^{+0.4}_{-0.3}$	$0.5^{+0.4}_{-0.2}$	$0.27^{+0.13}_{-0.12}$	[3]	0.72
GW170403	33 ± 7	48^{+9}_{-7}	$-0.7^{+0.5}_{-0.3}$	$0.7^{+0.2}_{-0.3}$	$0.45^{+0.22}_{-0.19}$	[3]	0.22
GW170817A	41 ± 7	⋯	$0.5^{+0.2}_{-0.2}$	0.7	$0.6^{+0.2}_{-0.2}$	[4]	0.17

Note. Note that reference [1] quotes the chirp masses in the source frame, whereas [2, 3] quote them in the detector frame, together with their respective errors (columns 2 and 3, respectively). For the events found by [2–4], we calculate the dispersion of the chirp mass in the source frame assuming no covariance between the parameters. $K_{\rm M1,\ obs,\ i}$ is the Bayes factor between model M1 and the observed distribution for each event i.

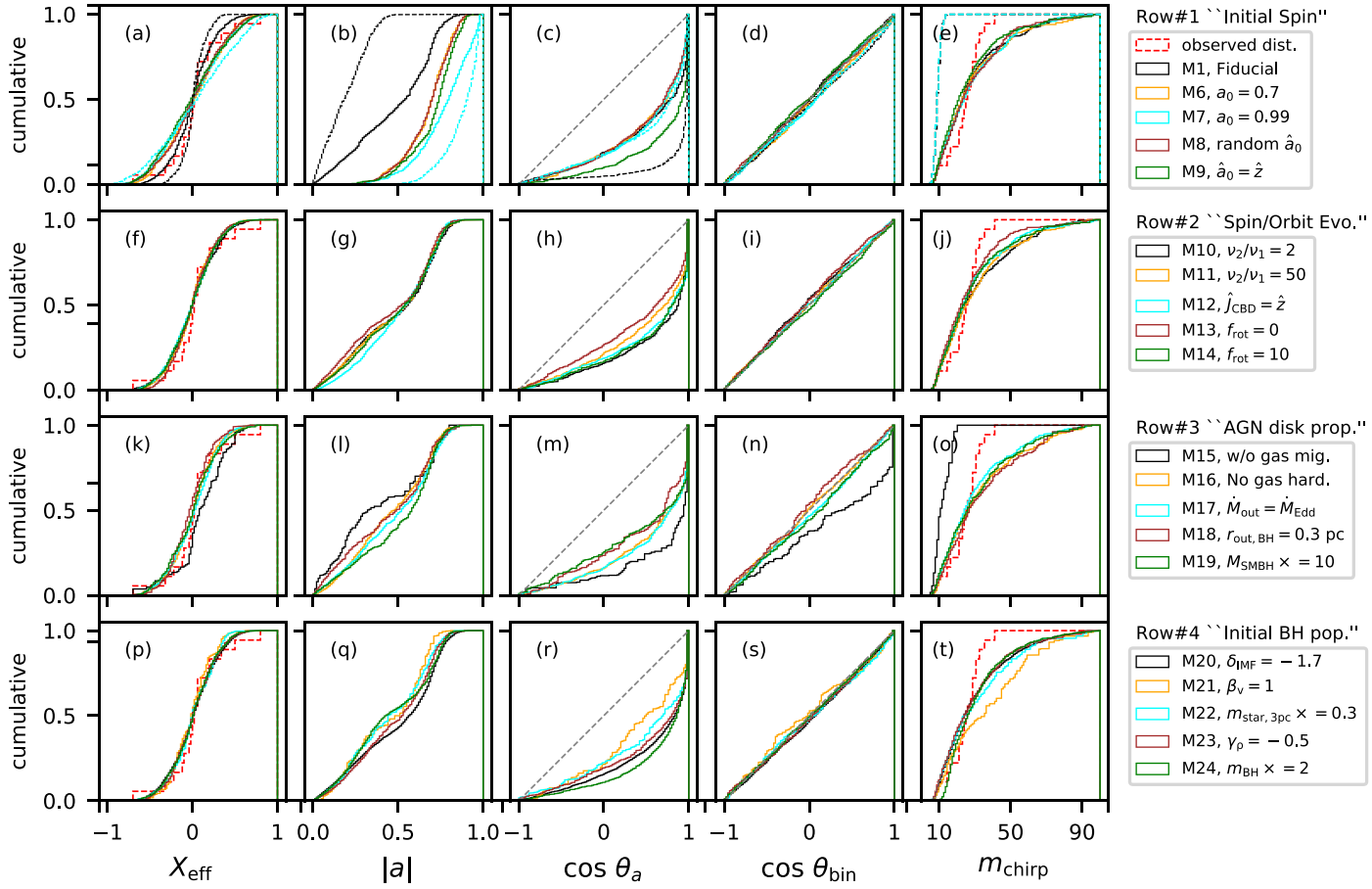

Figure 10. Same as Figure 3, but showing distributions without errors.

delivered to the nuclear star cluster by the infall of low-metallicity globular clusters where the BH masses are expected to be higher (Tremaine et al. 1975; Antonini 2013; Arca-Sedda et al. 2018; Arca Sedda & Benacquista 2019; Arca Sedda 2020). For a more rigorous comparison with the observed $m_{\rm chirp}$ distribution, these points should be considered in a future study.

Focusing only on the $\chi_{\rm eff}$ distribution, we find $P_{{\rm KS},\chi_{\rm eff}}$ are $\sim$0.1–0.7. This suggests that the observed $\chi_{\rm eff}$ distribution is consistent with most of our models. Figure 8 shows $P_{{\rm KS},\chi_{\rm eff}}$ (black lines) and $P_{{\rm KS,LV},\chi_{\rm eff}}$ (orange lines) as a function of $|a_0|$ (models M1–M7). The solid and dashed lines show the results in which observational errors are and are not included, respectively. $P_{{\rm KS},\chi_{\rm eff}}$ and $P_{{\rm KS,LV},\chi_{\rm eff}}$ are highest (0.68 and 0.15) in model M3 and M4, in which $|a_0| = 0.2$ and $|a_0| = 0.3$, respectively. Thus, moderate values for $|a_0|$ are preferred by the observed $\chi_{\rm eff}$ distribution.

We further investigate how the KS probabilities change if we assume that only some fraction $f_{\rm AGN} < 1$ of mergers occur in AGN disks, with the remaining fraction $(1 - f_{\rm AGN})$ produced in other unrelated channel(s). This gives an estimate for the maximum allowed fraction of events related to AGN disks in each of our models. For non-AGN mergers, we conservatively assume that the $\chi_{\rm eff}$ and $m_{\rm chirp}$ distributions are the same as the distributions observed to date (Table 3), but the detection rates are normalized to $(1 - f_{\rm AGN})$. On the other hand, for AGN mergers, each merger is weighted by the detectable volume referring to Kissel & Betzwieser (2018) as before, and the total detection rate distribution of $\chi_{\rm eff}$ and $m_{\rm chirp}$ in each model is normalized to $f_{\rm AGN}$.

We construct the $\chi_{\rm eff}$ and/or $m_{\rm chirp}$ distributions by summing non-AGN and AGN mergers, and calculating the KS probability of their combined distribution. The cyan, orange, and black lines in Figure 9 show $P_{{\rm KS},\chi_{\rm eff}}$, $P_{{\rm KS},m_{\rm chirp}}$, and $P_{{\rm KS},\chi_{\rm eff},m_{\rm chirp}}$ as a function of $f_{\rm AGN}$. The thick solid lines are the probabilities including all events (Table 3), and the dashed lines include only the events reported by the LIGO/Virgo groups (The LIGO Scientific Collaboration et al. 2019). Even for model M15, in which $P_{{\rm KS},\chi_{\rm eff},m_{\rm chirp}}$ is lowest for $f_{\rm AGN} = 1$, we find $P_{{\rm KS},\chi_{\rm eff},m_{\rm chirp}} \gtrsim 0.7$ provided that $f_{\rm AGN} \lesssim 0.30$ (solid black line in the right panel). Thus, at least $\sim$30% of mergers might originate in AGN disks even in the worst model (see discussion above on caveats that may increase $f_{\rm AGN}$ for model M15).

3.3.2. Bayesian Analysis

Next, to assess the relative likelihood of producing each event in different models, we calculate the Bayes factors between pairs of models,

$$K_{{\rm A,B},i} = \frac{P(d_i|{\rm A})}{P(d_i|{\rm B})} \tag{25}$$

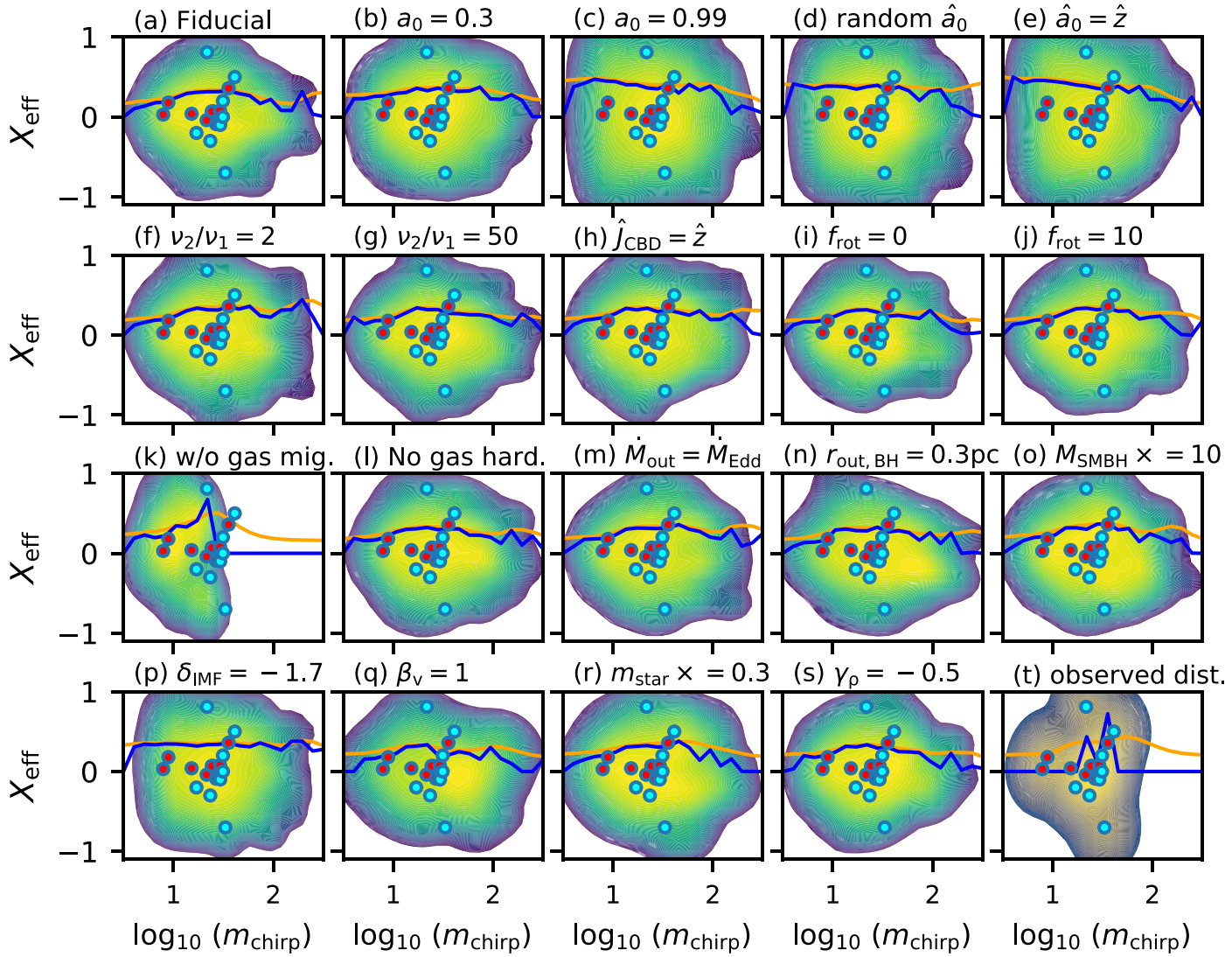

Figure 11. Same as Figure 4, but the standard deviations are presented. Blue lines show the standard deviation of the mergers in each bin, and orange lines show the standard deviation of the $\chi_{\rm eff}$ distribution, which is produced by performing a kernel-density estimate. The latter is shown as an estimate of the trend for the observed distribution in which the number of events is small.

where $P(d_i|{\rm A})$ is the likelihood of obtaining data d_i in an event i from Model A,

$$P(d_i|\ {\rm A}) = \int P(d_i|\ m_{\rm chirp},\ \chi_{\rm eff},\ q)\ P(m_{\rm chirp},\ \chi_{\rm eff},\ q|\ {\rm A})\ dm_{\rm chirp} d\chi_{\rm eff} dq \quad (26)$$

where $P(d_i|m_{\rm chirp},\ \chi_{\rm eff},\ q)$ is the three-dimensional likelihood for $m_{\rm chirp}$, $\chi_{\rm eff}$, and q, and $P(m_{\rm chirp},\ \chi_{\rm eff},\ q|{\rm A})$ is the probability distribution of $m_{\rm chirp}$, $\chi_{\rm eff}$, and q in Model A.

To calculate $P(m_{\rm chirp},\ \chi_{\rm eff},\ q|{\rm A})$, we first count mergers in $30 \times 30 \times 30$ uniform bins in $\chi_{\rm eff}$, $m_{\rm chirp}$, and q for Model A. The maximum and minimum values of $m_{\rm chirp}$ for the bins are set to 150 and $5\,M_\odot$, respectively. In this procedure, we weighted each merger by the detectable volume. To reduce the statistical fluctuation in the distribution of $\chi_{\rm eff}$, $m_{\rm chirp}$, and q due to the finite number of mergers in our models, we perform a kernel-density estimate for the distribution using Gaussian kernels whose bandwidth is chosen to satisfy Scott's rule (Scott 1992).

For simplicity, we assume that they follow independent Gaussian distributions, as commonly assumed in studies analyzing observed GW data (e.g., Fishbach & Holz 2017):

$$P(d_i|m_{\rm chirp},\ \chi_{\rm eff},\ q) \simeq N(m_{{\rm chirp},i},\ \sigma^2_{m_{{\rm chirp},i}}) N(\chi_{{\rm eff},i},\ \sigma^2_{\chi_{{\rm eff},i}}) N(q_i,\ {\sigma_{q,i}}^2), \quad (27)$$

where $N(c_1,\ {c_2}^2)$ is the Gaussian distribution with average c_1 and dispersion ${c_2}^2$, $m_{{\rm chirp},i}$, $\chi_{{\rm eff},i}$, and q_i are the median values and $\sigma^2_{m_{{\rm chirp},i}}$, $\sigma^2_{\chi_{{\rm eff},i}}$, and $\sigma^2_{q,i}$ are the dispersions of $m_{\rm chirp}$, $\chi_{\rm eff}$, and q observed in GW event i. We set the average values and the standard deviation for each event to the median values and the 90% credible intervals in Table 3 divided by 3.3, as appropriate for a Gaussian distribution. For the events found by the IAS group, for simplicity, we calculate the dispersion of the chirp mass in the source frame assuming no covariance between the parameters.

We calculate $P(d_i|m_{\rm chirp},\ \chi_{\rm eff},\ q)$ by generating 1000 samples according to the Gaussian distribution and normalizing

the distribution as

$$\frac{\int P(d_i|m_{\rm chirp},\,\chi_{\rm eff},\,q)\,dm_{\rm chirp}\,d\chi_{\rm eff}\,dq}{\int dm_{\rm chirp}\,d\chi_{\rm eff}\,dq}=1. \quad (28)$$

The values for $P(d_i|m_{\rm chirp},\,\chi_{\rm eff},\,q)$ are stored in $30\times30\times30$ uniform bins.

For each event i, we calculate the Bayes factor for a Model A relative to the observed distribution (i.e., "Model B" in the ratio in Equation (25) is taken to be the observed distribution itself). The observed distribution is constructed by smoothing the observed $m_{{\rm chirp},i}$, $\chi_{{\rm eff},i}$, and q_i distribution using a kernel-density estimate as applied above (Figure 4(t)). This $K_{{\rm A,obs},i}$ presents the strongest test of Model A for each event, since models are compared to the actual observed distribution.

In most models, the lowest value of $K_{{\rm A,obs},i}$ among the GW sources is typically $\sim$0.02–0.2 ($\min_i K_{{\rm A,obs},i}$ in Table 2), except for M15, in which it is much lower ($\sim10^{-5}$). In model M15, $K_{{\rm A,obs},i}$ is lowest for GW170817A, which is the source with the highest $m_{\rm chirp}$. These findings are consistent with Figure 4, which shows that the observed value for the event is outside the predicted range. For the fiducial model M1, we list the value of $K_{{\rm A,obs},i}$ for each observed source in Table 3. The most constraining event is GW151216 ($K_{{\rm A,obs},i}=0.050$); the source that has the highest $\chi_{\rm eff}$ (see also Huang et al. 2020). Thus, as expected, the events with the highest $\chi_{\rm eff}$ and $m_{\rm chirp}$ constrain the models most strongly.

3.4. Comparison to Other Formation Channels

In this section, we briefly discuss differences in the expected distributions of $\chi_{\rm eff}$ and/or $m_{\rm chirp}$ between the AGN disk-assisted channel and other binary merger channels.

First, our models with low $|a_0|$ produce the positive correlation between $m_{\rm chirp}$ and the dispersion of $\chi_{\rm eff}$ when $m_{\rm chirp}\lesssim20\,M_\odot$ (orange lines in Figures 5 and 11). Safarzadeh et al. (2020) estimated that the events reported by the LIGO/Virgo collaborations (The LIGO Scientific Collaboration et al. 2019) prefer a positive correlation with 80% confidence. Such correlation is somewhat more significant if the events reported by the IAS group are included (cyan circles in Figure 4). The evolution channels for field binaries likely favor rather negative correlation between $m_{\rm chirp}$ and the dispersion of $\chi_{\rm eff}$ (Gerosa et al. 2018; Bavera et al. 2020; Safarzadeh et al. 2020). The positive correlation is expected for repeated mergers, which frequently occur for multi-body systems in environments with a high escape velocity, such as galactic nuclei (Arca Sedda et al. 2020), and/or if initial BH spins are low (O'Leary et al. 2016). On the other hand, Arca Sedda et al. (2020) show that the positive correlation is not reproduced by mergers in dynamical environments. Hence, the positive correlation suggested by Safarzadeh et al. (2020) may be a signature that the observed mergers are facilitated in AGN disks.

Second, AGN disks can produce high-$m_{\rm chirp}$ mergers. For field binaries, $m_{\rm chirp}$ is limited to $\lesssim40\,M_\odot$ due to pair instability supernovae (e.g., Kinugawa et al. 2014; Spera et al. 2019). In the scenarios involving dynamical formation and evolution, Arca Sedda et al. (2020) predicted that 99% of mergers have $m_{\rm chirp}\lesssim50\,M_\odot$. For mergers in AGN disks, we find that $\sim$10%–15% of mergers have $m_{\rm chirp}\gtrsim50\,M_\odot$ if BHs migrate efficiently. Thus, if mergers with $m_{\rm chirp}\gtrsim50\,M_\odot$ are discovered, they would favor the AGN-disk origin. Although the false alarm rate is high (0.34 $\rm yr^{-1}$), Udall et al. (2019) reported a high-mass binary BH merger event, GW170502, with a chirp mass of $\sim70\,M_\odot$. Similar events with high signal-to-noise ratio will be an additional signature for mergers in AGN disks.

Third, if migration is inefficient (model M15), $\chi_{\rm eff}$ can be negative and the $\chi_{\rm eff}$ distribution may lack symmetry around $\chi_{\rm eff}=0$. From Table 2, the absolute value for the 90th percentiles for $\chi_{\rm eff}$ ($|\chi_{\rm eff,90}|$) is larger than that for the 10th percentiles ($|\chi_{\rm eff,10}|$) by $\sim$0.27 in this model. Such an asymmetric distribution of $\chi_{\rm eff}$ is caused by gas accretion, while it is reduced by the randomization of the binary angular momentum directions due to binary–single interactions.

Mergers in isolated environments are unlikely to produce negative $\chi_{\rm eff}$ (Bavera et al. 2020) unless angular momentum transfer is inefficient; however, in this case high-$\chi_{\rm eff}$ mergers are overproduced (Belczynski et al. 2020). Mergers in globular clusters and galactic nuclei (without AGN disks) can produce negative $\chi_{\rm eff}$, but the $\chi_{\rm eff}$ distribution is almost perfectly symmetric around $\chi_{\rm eff}=0$ (Rodriguez et al. 2018). Hence, if the asymmetric distribution is observed, a possible interpretation is that mergers originate in AGN disks and binary–single interactions are less efficient (e.g., due to inefficient inward migration to the densely populated inner regions).

In summary, the positive correlation between $m_{\rm bin}$ and the dispersion of $\chi_{\rm eff}$, high-$m_{\rm chirp}$ mergers, and an asymmetric $\chi_{\rm eff}$ distribution might be possible signatures that distinguish mergers in AGN disks from other channels. However, the $\chi_{\rm eff}$ and $m_{\rm chirp}$ distributions for mergers in AGN disks are found to be strongly affected by radial migration of BHs. The efficiency of this migration is still poorly understood, and should be investigated in the future.

3.5. Consistency with GW190412

Recently, an event with low mass ratio, GW190412, has been reported (The LIGO Scientific Collaboration and The Virgo Collaboration 2020). This is the first event that has a low mass ratio ($q=0.28^{+0.13}_{-0.07}$), is constrained to have nonzero BH spin parallel to the binary's orbital plane ($\chi_p=0.30^{+0.19}_{-0.15}$), has a primary BH with large spin ($a_1=0.43^{+0.16}_{-0.26}$), and is chosen from $\sim$50 triggers in the third observing run. Fishbach & Holz (2020) predicted that 99% of mergers have $q>0.51$ from the LIGO/Virgo events in O1/O2, which suggests that GW190412 is a highly unusual event. Gerosa et al. (2020) and Safarzadeh & Hotokezaka (2020) have shown that this event is exceedingly rare in both scenarios for mergers in isolated fields and globular clusters due to its low mass ratio and high projected spin component. Here, we suggest that the properties of GW190412 can be naturally explained by higher-generation mergers in an AGN disk. Due to the low mass ratio, we can expect that this may be a merger between a first-generation secondary BH with $M_2\approx8\,M_\odot$ and a second- (or higher-)generation primary BH with $M_1\approx30\,M_\odot$. Indeed, $q\sim0.28$ with $m_{\rm bin}\sim38\,M_\odot$ is common for mergers in AGN disks (see Figure 14 in Paper I). Furthermore, since mergers endow the remnant BH with high spin, the high value for the primary BH spin in GW190412 is consistent with it having experienced one or more prior mergers. Finally, in our models, the AGN disk delivers BHs to the inner regions where binary–single interactions frequently misalign the spins relative to the orbital angular momentum. If we include this event in the analysis in Section 3.3.2, the Bayes factor between model M1 and the observed distribution for GW190412 is 0.70, which

suggests that the AGN channel can naturally explain the properties of GW190412 well.

4. Conclusions

In this paper we have investigated the distribution of the effective spin parameter $\chi_{\rm eff}$ for BH binaries merging in accretion disks of AGNs. We performed one-dimensional *N*-body simulations, combined with semi-analytical prescriptions of the relevant processes. $\chi_{\rm eff}$ is enhanced by the alignment of BH spins toward the binary orbital angular momenta due to gas accretion, while it is reduced by the randomization of binary orbital angular momenta due to hard binary–single interactions. This is the first detailed estimate for the $\chi_{\rm eff}$ distribution of stellar-mass BH mergers in AGN disks, considering the effects of binary–single interactions and gas accretion. Our main results can be summarized as follows.

1. Due to the randomization of the binary orbital angular momentum directions by frequent binary–single interactions, $\chi_{\rm eff}$ is symmetric around zero if radial migration of BHs to the inner, densely populated regions is efficient. The median value of $|\chi_{\rm eff}|$ depends most strongly on the initial BH spin magnitudes and the efficiency of migration, and is much less impacted by the other parameters or prescriptions we considered.
2. The $\chi_{\rm eff}$ distribution for all observed events reported by the LIGO/Virgo collaborations and the IAS group during LIGO/Virgo O1 and O2 is roughly consistent with the distribution expected for mergers in AGN disks (Figure 6). The KS probabilities between the $\chi_{\rm eff}$ distribution of all events and those in our models are typically $\sim$0.1–0.7 ($P_{\rm KS,\chi_{eff}}$, Table 2). The observed $\chi_{\rm eff}$ distribution slightly favors moderate values for the initial BH spins ($|a_0| \lesssim 0.5$; see Figure 8).
3. Even for the worst-fitting model, the fractional contribution of mergers in AGN disks to all observed mergers is limited to only $\lesssim$0.3 (Figure 9), and much higher contributions are allowed in our other models.
4. The positive correlation between $m_{\rm chirp}$ and the dispersion of $\chi_{\rm eff}$ can be reproduced by AGN-assisted mergers if the initial BH spin magnitude is low (Figures 5 and 11, Section 3.4). Also, mergers in AGN disks might be distinguished from other channels based on the chirp masses extending to values as high as $\approx 300\,M_\odot$ (see also Paper I).
5. The properties of the recently announced gravitational-wave event, GW190412, including a low mass ratio, a high spin for the primary BH, and a spin component in the orbital plane, are naturally expected if it is a hierarchical merger in an AGN disk.

We thank Barry McKernan, Brian Metzger, Saavik Ford, and Leigh Nathan for useful discussions. This project has received funding from the European Research Council (ERC) under the European Union's Horizon 2020 research and innovation program under grant agreement No 638435 (GalNUC) and by the Hungarian National Research, Development, and Innovation Office grant NKFIH KH-125675. Z.H. acknowledges support from NASA grant NNX15AB19G and NSF grant 1715661. I.B. acknowledges the support of the Alfred P. Sloan Foundation and the University of Florida. Simulations and analyses were carried out on Cray XC50 and computers at the Center for Computational Astrophysics, National Astronomical Observatory of Japan.

ORCID iDs

Zoltán Haiman https://orcid.org/0000-0003-3633-5403
Imre Bartos https://orcid.org/0000-0001-5607-3637
Bence Kocsis https://orcid.org/0000-0002-4865-7517

References

Antonini, F. 2013, ApJ, 763, 62
Antonini, F., Toonen, S., & Hamers, A. S. 2017, ApJ, 841, 77
Arca Sedda, M. 2020, arXiv:2002.04037
Arca Sedda, M., & Benacquista, M. 2019, MNRAS, 482, 2991
Arca Sedda, M., Mapelli, M., Spera, M., Benacquista, M., & Giacobbo, N. 2020, ApJ, 891, 47
Arca-Sedda, M., Li, G., & Kocsis, B. 2018, arXiv:1805.06458
Banerjee, S. 2017, MNRAS, 467, 524
Barausse, E., Morozova, V., & Rezzolla, L. 2012, ApJ, 758, 63
Barausse, E., & Rezzolla, L. 2009, ApJL, 704, L40
Bardeen, J. M. 1970, Natur, 226, 64
Bartos, I., Haiman, Z., Marka, Z., et al. 2017a, NatCo, 8, 831
Bartos, I., Kocsis, B., Haiman, Z., & Márka, S. 2017b, ApJ, 835, 165
Baruteau, C., Cuadra, J., & Lin, D. N. C. 2011, ApJ, 726, 28
Baruteau, C., & Lin, D. N. C. 2010, ApJ, 709, 759
Bavera, S. S., Fragos, T., Qin, Y., et al. 2020, A&A, 635, A97
Belczynski, K., Bulik, T., Fryer, C., et al. 2010, ApJ, 714, 1217
Belczynski, K., Daniel, E. H., Bulik, T., & O'Shaughnessy, R. 2016, Natur, 534, 512
Belczynski, K., Klencki, J., Fields, C. E., et al. 2020, A&A, 636A, A104
Bellovary, J. M., mac Low, M. M., McKernan, B., & Ford, K. E. S. 2016, ApJ, 819, L17
Broz, M., Chrenko, O., Nesvornu, D., & Lambrechts, M. 2018, A&A, 620, A157
Burtscher, L., Meisenheimer, K., Tristram, K. R. W., et al. 2013, A&A, 558, 149
Chen, Y., Bressan, A., Girardi, L., et al. 2015, MNRAS, 452, 1068
Corley, K. R., Bartos, I., Singer, L. P., et al. 2019, MNRAS, 488, 4459
de Mink, S. E., & Mandel, I. 2016, MNRAS, 460, 3545
del Valle, L., & Volonteri, M. 2018, MNRAS, 480, 439
Derdzinski, A., D'Orazio, D., & Duffell, P. Z. H. A. M. 2019, MNRAS, 486, 2754
di Carlo, U. N., Giacobbo, N., Mapelli, M., et al. 2019, MNRAS, 487, 2947
Dominik, M., Belczynski, K., Fryer, C., et al. 2012, ApJ, 759, 52
D'Orazio, D. J., & Loeb, A. 2020, PhRvD, 101, 083031
Dubois, Y., Volonteri, M., & Silk, J. 2014, MNRAS, 440, 1590
Duffell, P. C., D'Orazio, D., Derdzinski, A., et al. 2019, arXiv:1911.05506
Duffell, P. C., Haiman, Z., MacFadyen, A. I., D'Orazio, D. J., & Farris, B. D. 2014, ApJL, 792, L10
Farr, W. M., Stevenson, S., Miller, M. C., et al. 2017, Natur, 548, 426
Farris, B. D., Duffell, P., MacFadyen, A. I., & Haiman, Z. 2014, ApJ, 783, 134
Fishbach, M., & Holz, D. E. 2017, ApJL, 851, L25
Fishbach, M., & Holz, D. E. 2020, ApJL, 891, L27
Ford, K. E. S., & McKernan, B. 2019, MNRAS, 490, L42
Fragione, G., & Kocsis, B. 2020, MNRAS, 493, 3920
Frank, J., King, A., & Raine, D. J. 2002, Accretion Power in Astrophysics (3rd ed.; Cambridge: Cambridge Univ. Press)
Freitag, M., Amro-Seoane, P., & Kalogera, V. 2006, ApJ, 649, 91
Fuller, J., & Ma, L. 2019, ApJL, 881, L1
Gammie, C. F., Shapiro, S. L., & McKinney, J. C. 2004, ApJ, 602, 312
Gayathri, V., Bartos, I., Haiman, Z., et al. 2020, ApJL, 890, L20
Gerosa, D., Berti, E., O'Shaughnessy, R., et al. 2018, PhRvD, 98, 084036
Gerosa, D., Lima, A., Berti, E., et al. 2019, CQGra, 36, 105003
Gerosa, D., Vitale, S., & Berti, E. 2020, arXiv:2005.04243
Gondán, L., Kocsis, B., Raffai, P., & Frei, Z. 2018, ApJ, 860, 5
Harding, B., Tremblay, C., & Cousineau, D. 2014, The Quantitative Methods for Psychology, 10, 107
Hopman, C., & Alexander, T. 2006, ApJL, 645, L133
Huang, Y., Haster, C.-J., Vitale, S., et al. 2020, arXiv:2003.04513
Inayoshi, K., Hirai, R., Kinugawa, T., & Hotokezaka, K. 2017a, MNRAS, 468, 5020
Inayoshi, K., Tamanini, N., Caprini, C., & Haiman, Z. 2017b, PhRvD, 96, 063014
Ivanova, N., Justham, S., Chen, X., et al. 2013, A&ARv, 21, 59

Kanagawa, K. D., Tanaka, H., & Szuszkiewicz, E. 2018, ApJ, 861, 140
Kesden, M., Sperhake, U., & Berti, E. 2010, PhRvD, 81, 084054
Keshet, U., Hopman, C., & Alexander, T. 2009, ApJL, 698, L64
King, A. R., Lubow, S. H., Ogilvie, G. I., & Pringle, J. E. 2005, MNRAS, 363, 49
Kinugawa, T., Inayoshi, K., Hotokezaka, K., & Nakauchi, D. T. N. 2014, MNRAS, 442, 2963
Kissel, J., & Betzwieser, J. 2018, LIGO Document, ligo-g 1802164-v1, https://dcc.ligo.org/LIGO-G1802164/public
Kocsis, B. 2013, ApJ, 763, 122
Kumamoto, J., Fujii, M. S., & Tanikawa, A. 2018, arXiv:1811.06726
Laughlin, G., Steinacker, A., & Adams, F. C. 2004, ApJ, 608, 489
Leigh, N. W. C., Geller, A. M., McKernan, B., et al. 2018, MNRAS, 474, 5672
Liu, B., & Lai, D. 2017, ApJL, 846, L11
Liu, B., & Lai, D. 2018, ApJ, 863, 68
Liu, B., Lai, D., & Wang, Y.-H. 2019, ApJ, 881, 41
Lodato, G., & Gerosa, D. 2013, MNRAS, 429, L30
Lousto, C. O., Zlochower, Y., Dotti, M., & Volonteri, M. 2012, PhRvD, 85, 084015
Lu, J. R., Do, T., Ghez, A. M., et al. 2013, ApJ, 764, 155
Lubow, S. H., Seibert, M., & Artymowicz, P. 1999, ApJ, 526, 1001
Mandel, I., & de Mink, S. E. 2016, MNRAS, 458, 2634
Mapelli, M., & Gualandris, A. 2016, LNP, 905, 205
Marchant, P., Langer, N., Podsiadlowski, P., Tauris, T., & Moriya, T. 2016, A&A, 588, A50
McKernan, B., Ford, K. E. S., Bellovary, J., et al. 2018, ApJ, 866, 66
McKernan, B., Ford, K. E. S., Kocsis, B., Lyra, W., & Winter, L. M. 2014, MNRAS, 441, 900
McKernan, B., Ford, K. E. S., Lyra, W., & Perets, H. B. 2012, MNRAS, 425, 460
McKernan, B., Ford, K. E. S., & O'Shaughnessy, R. 2020, arXiv:2002.00046
McKernan, B., Ford, K. E. S., O'Shaughnessy, R., & Wysocki, D. 2019, arXiv:1907.04356
Meiron, Y., Kocsis, B., & Loeb, A. 2017, ApJ, 834, 200
Miller, M. C., & Miller, J. M. 2015, PhR, 548, 1
Moody, M. S. L., Shi, J.-M., & Stone, J. M. 2019, ApJ, 875, 66
Neumayer, N., Seth, A., & Boeker, T. 2020, A&ARv, 28, 4
Nitz, A. H., Dent, T., Davies, G. S., et al. 2020, ApJ, 891, 123
Ogilvie, G. I. 1999, MNRAS, 304, 557
O'Leary, R. M., Kocsis, B., & Loeb, A. 2009, MNRAS, 395, 2127
O'Leary, R. M., Meiron, Y., & Kocsis, B. 2016, ApJL, 824, L12
Paczynski, B. 1976, in IAU Symp. 73, Structure and Evolution of Close Binary Systems, ed. S. Eggleton, P. Mitton, & J. Whelan (Dordrecht: Reidel), 75
Pavlovskii, K., Ivanova, N., Belczynski, K., & Van, K. X. 2017, MNRAS, 465, 2092
Portegies Zwart, S. F., & McMillan, S. L. W. 2000, ApJ, 528, L17
Press, W. H., & Teukolsky, S. A. 1988, ComPh, 2, 74
Qin, Y., Fragos, T., Meynet, G., et al. 2018, A&A, 616, A28
Rasskazov, A., & Kocsis, B. 2019, arXiv:1902.03242
Regan, J. A., Downes, T. P., Volonteri, M., et al. 2019, MNRAS, 486, 3892
Rezzolla, L., Barausse, E., Dorband, E. N., et al. 2008, PhRvD, 78, 044002
Rodriguez, C. L., Amaro-Seoane, P., Chatterjee, S., & Rasio, F. A. 2018, PhRvL, 120, 151101
Rodriguez, C. L., Chatterjee, S., & Rasio, F. A. 2016, PhRvD, 93, 084029
Safarzadeh, M., Farr, W. M., & Ramirez-Ruiz, E. 2020, ApJ, 894, 129
Safarzadeh, M., & Hotokezaka, K. 2020, ApJL, 897, L7
Samsing, J., MacLeod, M., & Ramirez-Ruiz, E. 2014, ApJ, 784, 71
Scott, D. 1992, Multivariate Density Estimation: Theory, Practice, and Visualization (New York: Wiley)
Secunda, A., Bellovary, J., mac Low, M.-M., et al. 2019, ApJ, 878, 85
Secunda, A., Bellovary, J., mac Low, M.-M., et al. 2020, arXiv:2004.11936
Shakura, N. I., & Sunyaev, R. A. 1973, A&A, 24, 337
Shapiro, S. L. 2005, ApJ, 620, 59
Shibata, M., & Shapiro, S. L. 2002, ApJL, 572, L39
Silsbee, K., & Tremaine, S. 2017, ApJ, 836, 39
Spera, M., Mapelli, M., Giacobbo, N., et al. 2019, MNRAS, 485, 889
Stevenson, S., Berry, C. P. L., & Mandel, I. 2017, MNRAS, 471, 2801
Stone, N. C., Metzger, B. D., & Haiman, Z. 2017, MNRAS, 464, 946
Szolgyen, A., & Kocsis, B. 2018, PhRvL, 121, 101101
Tagawa, H., Haiman, Z., & Kocsis, B. 2020, ApJ, 898, 25
Tagawa, H., Kocsis, B., & Saitoh, R. T. 2018, PhRvL, 120, 261101
Talbot, C., & Thrane, E. 2017, PhRvD, 96, 023012
The LIGO Scientific Collaboration and The Virgo Collaboration 2012, arXiv:1203.2674
The LIGO Scientific Collaboration and The Virgo Collaboration 2020, arXiv:2004.08342
The LIGO Scientific Collaboration and The Virgo Collaboration, Abbott, B. P., et al. 2019, PhRvX, 3, 031040
Thompson, T. A., Quataert, E., & Murray, N. 2005, ApJ, 630, 167
Thorne, K. S. 1974, ApJ, 191, 507
Tremaine, S. D., Ostriker, J. P., & Spitzer, L. J. 1975, ApJ, 196, 407
Udall, R., Jani, K., Lange, J., et al. 2019, arXiv:1912.10533
van den Heuvel, E. P. J., Portegies Zwart, S. F., & de Mink, S. E. 2017, MNRAS, 471, 4256
Venumadhav, T., Zackay, B., Roulet, J., Dai, L., & Zaldarriaga, M. 2019, arXiv:1904.07214
Vitale, S., Lynch, R., Sturani, R., & Graff, P. 2017, CQGra, 34, 03LT01
Volonteri, M., Sikora, M., & Lasota, J.-P. 2007, ApJ, 667, 704
Wong, K. W. K., Baibhav, V., & Berti, E. 2019, MNRAS, 488, 5665
Yang, Y., Bartos, I., Gayathri, V., et al. 2019a, PhRvL, 123, 181101
Yang, Y., Bartos, I., Haiman, Z., et al. 2019b, ApJ, 876, 122
Yang, Y., Bartos, I., Haiman, Z., et al. 2020, ApJ, 896, 138
Zackay, B., Dai, L., Venumadhav, T., Roulet, J., & Zaldarriaga, M. 2020, PhRvD, 101, 8
Zackay, B., Venumadhav, T., Dai, L., Roulet, J., & Zaldarriaga, M. 2019, PhRvD, 100, 023007